

A fast Huygens sweeping method for capturing paraxial multi-color optical self-focusing in nematic liquid crystals



Wingfai Kwan^a, Shingyu Leung^{a,*}, Xiao-Ping Wang^a, Jianliang Qian^b

^a Department of Mathematics, The Hong Kong University of Science and Technology, Clear Water Bay, Hong Kong

^b Department of Mathematics, Michigan State University, East Lansing, MI 48824, USA

ARTICLE INFO

Article history:

Received 17 March 2017

Received in revised form 10 June 2017

Accepted 8 July 2017

Available online 14 July 2017

Keywords:

Nematic liquid crystals

Partial differential equations

Parabolic wave equations

Numerical methods

Modeling

Nematicons

ABSTRACT

We propose a numerically efficient algorithm for simulating the multi-color optical self-focusing phenomena in nematic liquid crystals. The propagation of the nematicon is modeled by a parabolic wave equation coupled with a nonlinear elliptic partial differential equation governing the angle between the crystal and the direction of propagation. Numerically, the paraxial parabolic wave equation is solved by a fast Huygens sweeping method, while the nonlinear elliptic PDE is handled by the alternating direction explicit (ADE) method. The overall algorithm is shown to be numerically efficient for computing high frequency beam propagations.

© 2017 Elsevier Inc. All rights reserved.

1. Introduction

We propose an efficient numerical method to simulate light beams (the so-called nematicons) propagating inside a nematic liquid crystal (NLC). When the incident beam has a large enough intensity and frequency, the corresponding energy will reorientate the NLC cells. This change in the material property will then divert the motion of the incident beam, and sometimes it might even create self-focusing of the beam leading to a further concentration of energy. The self-focused spot, known as the focal spot, has its intensity and position affected by the settings. In many situations, this also leads to an off-axis meandering (undulation) which is then followed by a break-up (filamentation) of the beam. Because of these interesting unique optical and electrical properties, such a material has a wide range of applications from various types of display panel to telecommunication devices. We refer interested readers to [3,7] for a more complete introduction to the properties of NLC and the research field. Some experimental results can be found in [5,2].

Mathematically, we follow the discussion in [27] and model the orientation of the nematic field by an elliptic partial differential equation (PDE) while the optical field is governed by a paraxial parabolic wave equation with a nonlinear interaction with the underlying nematic field. Some analysis of this coupled nonlinear system can be found in, for example, [39,14]. This coupled nonlinear system can also be extended and applied to various related phenomenon including arbitrary degree of nonlinearity [10] and multi-color nematicons [36,37,35].

Numerically, it is challenging to solve the hyperbolic PDE in the high frequency regime. Since the high wavenumber in the parabolic wave equation introduces extremely rapid transverse oscillations across beams, typical direct methods such as finite-difference or finite-element methods require a very fine mesh to resolve the oscillations in the solution.

* Corresponding author.

E-mail addresses: wfkwan@ust.hk (W. Kwan), masyleung@ust.hk (S. Leung), mawang@ust.hk (X.-P. Wang), qian@math.msu.edu (J. Qian).

Because of the usual Courant–Fredrichs–Lewy condition for a hyperbolic-type PDE, the overall computational cost could be very high. An alternative to resolve these highly oscillatory wave function is to use asymptotic methods. In a series of studies [30,31,19,20], we have considered the geometrical optics approximation for acoustic wave equations and their corresponding inverse problems. In geophysical applications, Gaussian beam superpositions have been proposed for seismic wave modeling [9] and for seismic wave migration [13]. Based on [32,38], we have developed a purely Eulerian approach to compute the Gaussian beam solution in [23]. In the context of quantum mechanics where one has to solve the Schrödinger equation, some variants of Gaussian beams including the frozen Gaussian beams and Gaussian wave packets have been used to construct approximate solutions to the Schrödinger equation in the semi-classical regime [16,11,12]. However, these formulations were all based on the Lagrangian framework. In [21,22] we proposed an Eulerian formulation of Gaussian beams for the Schrödinger equation by generalizing [23,25]. We have recently proposed a novel method in [24], called the fast Huygens sweeping method, for solving the Schrödinger equation in the semi-classical regime [33,8] by incorporating the short-time Wentzel–Kramers–Brillouin–Jeffreys (WKBJ) propagator into Huygens’ principle. Even though the WKBJ solution is valid only for a short time period due to the occurrence of caustics, the Huygens’ principle allows us to construct the global-in-time semi-classical solution. To further improve the computational efficiency, we have developed in [24] analytic approximation formulas for the short-time WKBJ propagator by using the Taylor expansion in time.

There are two main contributions in this paper. We notice that the original Huygens sweeping method as proposed in [24] has a lower bound in the step size for time. This will hinder a detailed visualization of the beam self-focusing and interaction. In the first part of the paper, we will propose a simple strategy to relax the lower bound on the time marching step using a forward-backward step marching approach. In the second part of the work, we will replace the simple iterative solver for the nematic field as discussed in [27] by the alternative direction explicit (ADE) method [18]. The method has been shown to be unconditionally stable for elliptic type problems and, therefore, it is computationally extremely efficient for our application. In the example section, we are going to demonstrate that the computational complexity of our proposed approach is of order of approximately $O(N^d)$ where N is the number of grid points used in each of the physical direction and d is the overall dimension of the problem. Because of this improvement in the computational efficiency, we are now able to carry out detailed studies of the behavior of multiple frequency wave propagations in nonlinear media like NLC even in high dimensions.

The rest of the paper is organized as follows. In Section 2, we will briefly summarize the background of the project and some necessary components of the proposed algorithm. With these new developments in the numerical algorithm for different equations, we propose in Section 3 an efficient implementation for modeling the propagation of beams with multiple colors in nematic liquid crystals.

2. Background

In this section, we will summarize the mathematical formulation for modeling the nematic liquid crystals. Then we will introduce briefly two numerical methods including the fast Huygens sweeping method and the alternating direction explicit (ADE) method in the following subsections which will be the building blocks of the overall algorithm.

2.1. A paraxial model for multi-color optical self-focusing

As suggested by [27], the paraxial model represents a particular form and inherits features from the actual time-independent electromagnetic wave and nematic liquid crystal model. We consider the time-harmonic vectorial Maxwell’s equations and the static Frank free-energy nematic equation [39]:

$$\begin{aligned} \nabla \times \nabla \times \mathbf{E} - k^2[\mathbf{E} + \alpha(\mathbf{n} \cdot \mathbf{E})\mathbf{n}] &= 0, \\ \mathbf{n} \times [(\Delta\mathbf{n}) + (\mathbf{n} \cdot \mathbf{E}^*)\mathbf{E} + (\mathbf{n} \cdot \mathbf{E})\mathbf{E}^*] &= 0, \end{aligned}$$

with simplification made by imposing the *paraxial substitution* [28]:

$$\mathbf{E} = \begin{pmatrix} U \\ 0 \\ H \end{pmatrix} e^{ikz} \text{ and } \mathbf{n} = \begin{pmatrix} \sin\theta \\ 0 \\ \cos\theta \end{pmatrix}.$$

Assuming that the wavenumber $k \gg 1$ is large with a slowly varying envelope approximation in a medium with small anisotropy α , we can conclude that the longitudinal electric field H becomes negligible compared to the transverse component U . Let θ be the nematic field representing the angles between the NLC rod-like cells and the direction of propagation (z in our case) [6]. We have

$$2ik \frac{\partial}{\partial z} U + (\Delta_{\perp} + k^2 \alpha \sin^2 \theta) U = 0, \tag{1}$$

$$\left(\frac{\partial}{\partial z^2} + \Delta_{\perp} \right) \theta + |U|^2 \sin 2\theta = 0, \tag{2}$$

with the initial conditions $U(x, z = 0) = U_0(x)$ and $\theta(x, z = 0) = 0$. We impose the following Dirichlet boundary conditions: $U(x_{\min}, z) = U(x_{\max}, z) = 0$ and $\theta(x_{\min}, z) = \theta(x_{\max}, z) = 0$. For the nonlinear elliptic equation, we further set $\theta_z(x, z_{\max}) = 0$.

This model is widely used in [29,15]. We refer interested readers to [6] for the experimental set-up and [27,26] for the analysis of the model. The coupled model is nonlinear leading to the self-focusing effects of U .

In this paper, we model multiple color optical beam propagations inside the NLC. Let $U^{(j)}$ be the optical fields for beams with different frequencies labeled by j . While the evolution of each individual beams satisfies a parabolic wave equation, these equations are coupled through a nonlinear elliptic PDE [1,36,37,35]. The system is as follows:

$$2ik_j \frac{\partial}{\partial z} U^{(j)} + (\Delta_{\perp} + k_j^2 \alpha \sin^2 \theta) U^{(j)} = 0 \text{ for } j = 1, \dots, n, \tag{3}$$

$$\left(\frac{\partial^2}{\partial z^2} + \Delta_{\perp} \right) \theta + \left(\sum_j \beta_j |U^{(j)}|^2 \right) \sin 2\theta = 0, \tag{4}$$

where $k_j \gg 1$ is the non-dimensionalized wave number for each individual beams, α measures the refractive anisotropy, β_j are weights measuring the coupling between the light and the nematic for different colors, and Δ_{\perp} is the Laplacian in the subspace perpendicular to the z -direction. While only one beam is considered, setting $j = 1$ recovers the paraxial model (1) and (2). Besides the nonlinearity from each individual beam alone, the initial position is another factor affecting the self-focusing effect. Numerical examples will be shown in Section 4.2.5.

2.2. The fast Huygens sweeping method for the Schrödinger equation in the semi-classical Regime

In this section, we briefly summarize a recently developed method [24] to compute the highly oscillatory solution of the Schrödinger equation for a particle with unity mass given by

$$\left(i\hbar \frac{\partial}{\partial t} - H \right) U \equiv i\hbar U_t - V(x)U + \frac{\hbar^2}{2} \Delta U = 0$$

with the initial condition $U(x, t_0) = U_0(x)$. For the details of the numerical algorithm, we refer interested readers to [24].

The Green's function $G(x, t; x_0, t_0)$ of the partial differential equation [34,24] solves the following homogeneous initial value problem:

$$\left(i\hbar \frac{\partial}{\partial t} - H \right) G(x, t; x_0, t_0) = 0, \quad x \in \mathbb{R}^d, \quad t > t_0,$$

$$\lim_{t \rightarrow t_0^+} G(x, t; x_0, t_0) = \delta(x - x_0), \quad x \in \mathbb{R}^d,$$

$$G(x, t; x_0, t_0) = 0, \quad x \in \mathbb{R}^d, \quad t < t_0,$$

where (x_0, t_0) are parameters, and the Hamiltonian H takes the form of kinetic-plus-potential form: $H = -\frac{\hbar^2}{2} \frac{\partial^2}{\partial x^2} + V(x)$. Therefore, $G(x, t; x_0, t_0)$ can be seen as the response at position x and time t due to a point source at position x_0 and time t_0 . According to the Huygens' principle, the wave function $U(x, t)$ for $t > t_0$ for the Schrödinger equation can be written as

$$U(x, t) = \int_{\mathbb{R}^d} G(x, t; x_0, t_0) U(x_0, t_0) dx_0, \quad t > t_0,$$

which formalizes the fact that the superposition of waves radiating from each point of an old wave creates a new wave at a later time, and the Green's function provides appropriate weighting factors for the superposition. The above facts are well known in quantum mechanics; see [34].

The initial condition for the Green's function is a superposition of plane waves. In order to obtain needed ingredients in the asymptotic form of Green's functions, we will solve the following eikonal and transport equations:

$$\tau_t + V(x) + \frac{1}{2} |\nabla \tau|^2 = 0, \quad t > t_0, \tag{5}$$

$$\tau(x, t_0; \xi) = x \cdot \xi,$$

$$A_t + \nabla \tau \cdot \nabla A + \frac{1}{2} \Delta \tau A = 0, \quad t > t_0, \tag{6}$$

$$A(x, t_0; \xi) = 1,$$

where $\xi \in \mathcal{R}^d$ is a parameter, which can be viewed as a momentum variable as corresponding to x as a position variable. According to the PDE theory on the Hamilton–Jacobi equation, the eikonal equation (5) has a unique smooth solution for a short period of time; we denote this short period of time as $[t_0, t_0 + T]$, where $T > 0$ is a constant.

For the asymptotic Green's function G (without confusion still denoted as G), we assemble these computed ingredients into the following formula,

$$G(x, t; x_0, t_0) = \left(\frac{1}{2\pi\hbar}\right)^d \int_{\mathbb{R}^d} A(x, t; \xi) e^{\frac{i(\tau(x,t;\xi) - x_0 \cdot \xi)}{\hbar}} d\xi.$$

This $G(x, t; x_0, t_0)$ satisfies the Schrödinger equation asymptotically in the time period $t_0 \leq t \leq t_0 + T$ and satisfies the corresponding point-source initial condition. With the asymptotic Green's function at our disposal, we can propagate an arbitrary initial wave function $U(x, t_0)$ for a short period of time,

$$U(x, t) = \int_{\mathbb{R}^d} G(x, t; x_0, t_0) U(x_0, t_0) dx_0, \quad t_0 < t \leq t_0 + T. \tag{7}$$

Now since the Hamiltonian is time independent, the Green's function satisfies the following property,

$$G(x, t; x_0, t_0) = G(x, t_1; x_0, t_2) \quad \text{if } t - t_0 = t_1 - t_2 > 0.$$

This implies that the short-time-valid Green's function can be repeatedly used to propagate the wave function for long time,

$$U(x, t) = \int_{\mathbb{R}^d} G(x, t; x_0, t_n) U(x_0, t_n) dx_0, \quad t_n < t \leq t_n + T,$$

where $t_n = t_0 + (n - 1)T$ for $n = 1, 2, \dots$. This way we may sweep through a long period of time so that we may obtain global-in-time asymptotic solutions for the Schrödinger equation. For small time Δt , we can approximate the eikonals and amplitudes using Taylor expansion in time:

$$\begin{aligned} A(x, \Delta t; \xi) &= 1 + A_1(x, \xi)\Delta t + A_2(x, \xi)\Delta t^2 + O(\Delta t^3), \\ \tau(x, \Delta t; \xi) &= x \cdot \xi + \tau_1(x, \xi)\Delta t + \tau_2(x, \xi)\Delta t^2 + O(\Delta t^3). \end{aligned} \tag{8}$$

See [Appendix A](#) for a recursive derivation of these terms. Theoretically, we can incorporate more terms into our algorithm to obtain higher-order approximations. However, for our purpose, we concentrate on the lower-order case.

Taking only the leading order terms in the expansion, we approximate the asymptotic Green's function by

$$\begin{aligned} G(x, \Delta t; x', 0) &\simeq \left(\frac{1}{2\pi\hbar}\right)^d \int_{\mathbb{R}^d} e^{\frac{i}{\hbar} [x \cdot \xi - (V(x) + \frac{1}{2}|\xi|^2)\Delta t - x' \cdot \xi]} d\xi \\ &= \frac{1}{(i2\pi\hbar\Delta t)^{d/2}} \exp\left[\frac{-i}{\hbar} V(x)\Delta t\right] \exp\left[\frac{i}{2\hbar\Delta t} |x - x'|^2\right]. \end{aligned}$$

As a result, the integral (7) can be approximated by

$$\begin{aligned} U(x, \Delta t) &= \int_{\mathbb{R}^d} G(x, \Delta t; x', 0) U(x', 0) dx' \\ &\simeq \frac{1}{(i2\pi\hbar\Delta t)^{d/2}} \exp\left[\frac{-i}{\hbar} V(x)\Delta t\right] \int_{\mathbb{R}^d} \exp\left[\frac{i}{2\hbar\Delta t} |x - x'|^2\right] U(x', 0) dx'. \end{aligned}$$

We can take advantage of the special structure to compute the convolution efficiently using FFT. For simplicity we only discuss the numerical procedure in 1D and it is straight-forward to extend the approach to higher dimensions. We first approximate the integral on a uniform mesh x_i using the Trapezoidal rule, i.e.

$$U(x_i, \Delta t) = \frac{1}{(i2\pi\hbar\Delta t)^{1/2}} \exp\left[\frac{-i}{\hbar} V(x_i)\Delta t\right] \Delta x \sum_j \exp\left[\frac{i}{2\hbar\Delta t} |x_i - x_j|^2\right] U(x_j, 0). \tag{9}$$

In the form of matrix-vector multiplication, we denote the summation by a symmetric Toeplitz matrix \mathbf{W} with each entry given by $W_{i,j} = \exp\left[\frac{i}{2\hbar\Delta t} |x_i - x_j|^2\right]$.

Numerically, Δt in this approximation cannot be arbitrarily chosen. To resolve the oscillations in the coefficients of $W_{i,j}$, we require that the phase difference between $W_{1,N-1}$ and $W_{1,N}$ should be less than 2π , i.e. we require

$$\frac{[(N - 1)^2 - (N - 2)^2]\Delta x^2}{2\hbar\Delta t} = \alpha 2\pi$$

for some $0 < \alpha < 1$, which implies the following bound on Δt ,

$$\Delta t > \Delta t^* = \frac{(2N-3)\Delta x^2}{4\pi\hbar} = O\left(\frac{\Delta x}{\hbar}\right). \quad (10)$$

Note that this constraint imposes a **lower** bound on the marching step size Δt . For a given \hbar and Δx , the method requires one to pick a large enough Δt in order to resolve the oscillations in $W_{i,j}$. Indeed the larger the value of Δt , the faster we reach the final solution. However, we have to control the error introduced in the Taylor approximation at the same time. Therefore, we pick α close to, but smaller than, 1.

2.3. The Alternating Direction Explicit (ADE) method for the linear heat equation

We consider solving the one-dimensional heat equation

$$\frac{\partial T}{\partial t} = \frac{\partial^2 T}{\partial x^2}$$

with the boundary condition $T(x_0, t) = T_0$ and $T(x_{N+1}, t) = T_{N+1}$ and the initial condition $T(x_i) = T_i$. The ADE scheme [17, 4,18] is a numerical scheme which is unconditionally stable and second-order accurate in both space and time. The method is given by the following simple explicit iteration:

Algorithm (ADE for one dimensional heat equation).

1. Set $u_i^n = T_i^n$ and $v_i^n = T_i^n$ for $i = 1, \dots, N$;
2. For $i = 1, 2, \dots, N$, solve

$$\frac{u_i^{n+1} - u_i^n}{\Delta t} = \frac{u_{i-1}^{n+1} - u_i^{n+1} - u_i^n + u_{i+1}^n}{\Delta x^2}; \quad (11)$$

3. For $i = N, N-1, \dots, 1$, solve

$$\frac{v_i^{n+1} - v_i^n}{\Delta t} = \frac{v_{i-1}^n - v_i^n - v_i^{n+1} + v_{i+1}^{n+1}}{\Delta x^2}; \quad (12)$$

4. Compute

$$T_i^{n+1} = \frac{u_i^{n+1} + v_i^{n+1}}{2}.$$

Note that according to the index sweeping procedures in step 2 and step 3, both u_i^{n+1} and v_i^{n+1} are computed explicitly. When we calculate u_i^{n+1} in step 2, because the index is in the ascending order, we have already known the value u_{i-1}^{n+1} on the right hand side of (11). Similarly, when we calculate v_i^{n+1} in step 3, because the index is in the descending order, we have already known the value v_{i+1}^{n+1} on the right hand side of (12). As a result, the whole method is fully explicit. More importantly, the stability analysis shows that this numerical scheme is unconditionally stable for all $\Delta t > 0$. We refer interested readers to [18] for a more detailed discussion and analysis of the numerical method.

3. The proposed algorithm

In this section, we propose modifications to the original algorithm developed in [27] to improve the overall computational efficiency. The first modification is to replace the standard finite difference method by the newly developed fast Huygens sweeping method for the parabolic wave equations. The original fast Huygens sweeping method, however, does not completely fit the current application due to the existence of a lower bound (10) on the marching step size. To better resolve the self-focusing and intersection of the beams, we first propose a modification to the original scheme based on the time-reversibility property of the partial differential equation. The second modification of the overall algorithm is to replace the original SOR method by the ADE approach. The overall computational procedure is summarized as follows, while the implementation details are given in the following subsections.

Overall Algorithm 2.

1. Set a fine mesh for U and a coarse mesh for θ . Denote their corresponding number of mesh points N_x and N_θ , respectively. Initialize these functions on their corresponding meshes.
 2. $k = k + 1$.
 3. Interpolate θ on the fine mesh from N_θ points to N_x points.
 4. (Section 3.1) Compute $U^{(j)}$ in (3) using the fast Huygens sweeping method on the fine mesh.
 5. (Section 3.2) Compute θ in (4) using the ADE method on the coarse mesh with number of mesh points N_θ .
 6. Repeat step 2 until steady state.
-

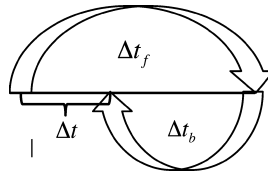


Fig. 1. A simple strategy to determine the solution at $t \in (0, \Delta t^*]$ using the initial condition imposed at $t = 0$.

3.1. A modified algorithm for the parabolic wave equation

As discussed before, the original Huygens sweeping method has a lower bound in the step size, which hinders a detailed visualization of the beam self-focusing and interaction. To demonstrate the effect of this lower bound on visualizing the evolution, we consider the following simple example which tried to demonstrate how two free Gaussian pulses ($V \equiv 0$) move towards each other and interact when they coincide. In this case we are considering $V(x) = 0$ with $\hbar = 2^{-17}$ and $N = 2^{17}$. The initial condition is

$$\psi(x, 0) = \frac{1}{\sqrt{\sqrt{\pi}d^2}} \left[\exp\left(-\frac{(x-x_-)^2}{2d^2}\right) \exp\left(\frac{ixp_+}{\hbar}\right) + \exp\left(-\frac{(x-x_+)^2}{2d^2}\right) \exp\left(\frac{ixp_-}{\hbar}\right) \right],$$

where $p_{\pm} = \pm 0.1$, $x_{\pm} = \pm 0.25$, and $d = 0.1$. Furthermore, we have $\Delta t^* = 5$ when we apply the lower bound mentioned in (10). The numerical solutions are shown in Example 4.1.2. As seen in the numerical solution, one can hardly resolve the interaction of the two Gaussians.

3.1.1. A first attempt

We propose in this section a simple improvement to compute the solution at the time between zero and the lower bound. The idea is based on the fact that the Schrödinger equation is time-reversible and the Taylor expansion approximation (8) holds even for a backward timestep with $-\Delta t < 0$. In particular, given the terminal condition $U(x_i, 0)$ at $t = 0$, the solution at $t = -\Delta t$ obtained using the same numerical scheme as in equation (9) given by

$$U(x_i, -\Delta t) = \frac{1}{(-i2\pi\hbar\Delta t)^{\frac{1}{2}}} \exp\left[\frac{i}{\hbar}V(x_i)\Delta t\right] \Delta x \sum_j \exp\left[-\frac{i}{2\hbar\Delta t}|x_i - x_j|^2\right] U(x_j, 0). \tag{13}$$

Even though the backward step has the same stability condition given by $\Delta t > \Delta t^*$, a composition of a forward step followed by a backward step allows one to resolve the solution between 0 and Δt^* . We denote $\Delta t_f > 0$, $\Delta t_b < 0$ and Δt to be the forward step, backward step and the desired time-mesh size, respectively. To obtain the solution at $\Delta t \in (0, \Delta t^*]$ using the initial condition at $t = 0$, we first march the solution for $\Delta t_f = \Delta t + \Delta t_b > \Delta t^*$ forward in time. Then, we apply the same numerical scheme but backward in time by Δt_b . The overall marching will finally be of the size $\Delta t_f - \Delta t_b = (\Delta t + \Delta t_b) - \Delta t_b = \Delta t$, as illustrated in Fig. 1.

The convergence of this simple proposed scheme depends not only on Δt alone but clearly also on our choices of Δt_f and Δt_b . In particular, the error E due to the approximation from the Taylor expansion is given by

$$\begin{aligned} E &= \left[O((\Delta t_f)^2) + O((\Delta t_b)^2) \right] \cdot (\text{Number of time marching}) \\ &= \left[O((\Delta t + \Delta t_b)^2) + O((\Delta t_b)^2) \right] \cdot \frac{T}{\Delta t} = O\left[\frac{(\Delta t_b)^2}{\Delta t} + \Delta t_b + \Delta t\right] \end{aligned}$$

where T is the final time in the domain. Since $\Delta t_b = O(\Delta t^*)$, the overall error in the numerical solution might actually grow if we try to visualize the solution using a finer time resolution (as we reduce Δt). One resolution to this is to reduce Δx at the same time as Δt approaches zero by picking $\Delta t = O(\Delta x)$. Since $\Delta t_b = O(\Delta t^*) = O(\Delta x)$, we have that the error E converges to zero.

Similar to the original algorithm, this modified marching strategy preserves the position density of the Schrödinger equation. We present it as the theorem below.

Theorem 3.1. *The numerical solution computed by the modified algorithm satisfies*

$$\int_x |U(x, \Delta t)|^2 dx = \int_x |U(x, 0)|^2 dx$$

for $\Delta t \in (0, \Delta t^*)$.

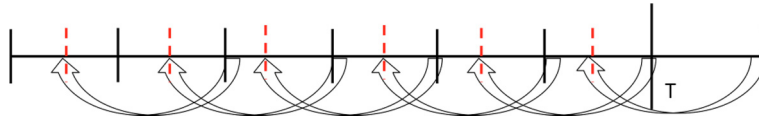


Fig. 2. The proposed strategy to determine the solution at arbitrary time between the initial time and the final time T . The black marks are the discrete time where the solutions computed using the original method where the time is marching forward in time. To fill in the gap between the solutions, we apply the original scheme backward in time as marked by red markers.

The proof is similar to the one stated in [24]. One first shows that

$$\int_x |U(x, 0)|^2 dx = \int_x |U(x, \Delta t_f)|^2 dx = \int_x |U(x, \Delta t_f - \Delta t_b)|^2 dx = \int_x |U(x, \Delta t)|^2 dx,$$

and then the result follows.

3.1.2. An efficient implementation

Indeed the above algorithm can resolve the solution using a smaller time step by relaxing the lower bound (10). The approach, on the other hand, significantly increases the error due to the Taylor expansion since the error is cumulative in the time marching. To reduce the error in the final solution, intuitively we need to avoid the coupling between the forward and the backward steps. In this proposed numerical scheme, we first compute the global-in-time solution using the forward step (9) until the final time T . This step is the same as discussed in [24]. Then we fill the gap in the timeline between two adjacent time steps using the backward step (13) as discussed before. Fig. 2 shows systematically how the scheme works.

3.2. An ADE method for the nematic field

In this section, we consider various numerical approaches to the elliptic equation for the nematic field. We recall that the coupled system does not in general guarantee the uniqueness in the solution. In particular, the nonlinear elliptic equation (2) has a trivial solution $\theta = 0$. Furthermore, it is still an important open question to answer whether the non-trivial solution to the nonlinear system is a unique one. Therefore, if we apply the typical Newton-type approach to the elliptic equation to solve the nonlinear system, the iteration will converge to a solution depending on the initial condition and also the Jacobian of the system. We will demonstrate this later in Section 4.2.1.

Instead, we introduce an artificial time t to the nematic equation and look for the steady state solution,

$$\frac{\partial \theta}{\partial t} = \left(\frac{\partial^2}{\partial z^2} + \Delta_{\perp} \right) \theta + |U|^2 \sin 2\theta, \tag{14}$$

for a given intermediate solution $U = U^k$ to the parabolic wave equation. The initial condition for this artificial time-dependent equation is given by $\theta(x, z, t = 0) = 1$ for interior points in the computational domain while the boundary condition satisfies the original boundary condition for the nonlinear elliptic equation, i.e. $\theta(x, z, t) = 0$. Clearly an explicit time marching method will be undesirable since we are looking for the solution at a large time. To design a computationally efficient approach, one might discretize the equation using an implicit method. For example, applying the backward Euler method in time, we obtain $\tilde{\theta}^{n+1}$ by solving

$$(I - \Delta t \Delta) \tilde{\theta}^{n+1} = \tilde{\theta}^n + \Delta t |U|^2 \sin 2\tilde{\theta}^n \tag{15}$$

with the initial condition $\tilde{\theta}^0 = \theta^{k-1}$ and n is the index for the iteration corresponding to the artificial time t . Once we have the steady state solution, we assign $\theta^k = \tilde{\theta}^{\infty}$. To invert the linear operator $(I - \Delta t \Delta)$, one can use any well-developed method like SOR method or alternating direction implicit (ADI) scheme or preconditioned conjugate gradient (PCG) based on FFT. However, instead of implementing these methods, we propose to use the ADE method which is unconditionally stable yet explicit. The algorithm is shown below.

Algorithm (ADE for two dimensional nematic equation).

1. Initialize $n = 0$.
2. Set $u_{i,j}^n = \theta_{i,j}^n$, $v_{i,j}^n = \theta_{i,j}^n$, $w_{i,j}^n = \theta_{i,j}^n$ and $r_{i,j}^n = \theta_{i,j}^n$ for $i, j = 1, \dots, N$;
3. For $i = 1, 2, \dots, N$ and $j = 1, 2, \dots, N$, solve

$$\frac{u_{i,j}^{n+1} - u_{i,j}^n}{\Delta t} = \frac{u_{i-1,j}^{n+1} - u_{i,j}^{n+1} - u_{i,j}^n + u_{i+1,j}^n}{\Delta x^2} + \frac{u_{i,j-1}^{n+1} - u_{i,j}^{n+1} - u_{i,j}^n + u_{i,j+1}^n}{\Delta z^2} + |U_{i,j}|^2 \sin 2\theta_{i,j}^n;$$

4. For $i = N, N - 1, \dots, 1$ and $j = N, N - 1, \dots, 1$, solve

$$\frac{v_{i,j}^{n+1} - v_{i,j}^n}{\Delta t} = \frac{v_{i-1,j}^n - v_{i,j}^n - v_{i,j}^{n+1} + v_{i+1,j}^{n+1}}{\Delta x^2} + \frac{v_{i,j-1}^n - v_{i,j}^n - v_{i,j}^{n+1} + v_{i,j+1}^{n+1}}{\Delta z^2} + |U_{i,j}|^2 \sin 2\theta_{i,j}^n;$$

5. For $i = 1, 2, \dots, N$ and $j = N, N - 1, \dots, 1$, solve

$$\frac{w_{i,j}^{n+1} - w_{i,j}^n}{\Delta t} = \frac{w_{i-1,j}^{n+1} - w_{i,j}^{n+1} - w_{i,j}^n + w_{i+1,j}^n}{\Delta x^2} + \frac{w_{i,j-1}^{n+1} - w_{i,j}^{n+1} - w_{i,j}^n + w_{i,j-1}^n}{\Delta z^2} + |U_{i,j}|^2 \sin 2\theta_{i,j}^n;$$

6. For $i = N, N - 1, \dots, 1$ and $j = 1, 2, \dots, N$, solve

$$\frac{r_{i,j}^{n+1} - r_{i,j}^n}{\Delta t} = \frac{r_{i+1,j}^{n+1} - r_{i,j}^{n+1} - r_{i,j}^n + r_{i-1,j}^n}{\Delta x^2} + \frac{r_{i,j-1}^{n+1} - r_{i,j}^{n+1} - r_{i,j}^n + r_{i,j+1}^n}{\Delta z^2} + |U_{i,j}|^2 \sin 2\theta_{i,j}^n;$$

7. Compute

$$\theta_i^{n+1} = \frac{u_{i,j}^{n+1} + v_{i,j}^{n+1} + w_{i,j}^{n+1} + r_{i,j}^{n+1}}{4}.$$

8. Set $n = n + 1$ and go to step 2 until converges.
-

4. Numerical examples

In the following sections, we are going to demonstrate the effect of the modification made in the fast Huygens sweeping method and also the application to NLC modeling. In Section 4.1, we will consider the linear Schrödinger equation and demonstrate the use of the modification made in the Fast Huygen sweeping method. Then we will illustrate the numerical solutions of 2D and 3D paraxial models in Section 4.2 and Section 4.3, respectively.

4.1. Examples on the modified fast Huygens sweeping method

4.1.1. Single free-space Gaussian

In this case, we apply the modified fast Huygens sweeping method to simulate the evolution of a free space Gaussian, i.e. $V(x) = 0$ and with an initial condition given by

$$\psi(x, 0) = \frac{1}{\sqrt{\sqrt{\pi}d^2}} \exp\left(-\frac{(x - x_0)^2}{2d^2}\right) \exp\left(\frac{ixp_0}{\hbar}\right)$$

where $p_0 = 0.1$, $d = 0.1$ and $x_0 = -0.5$. We consider $\hbar = 2^{-16}$ with final time $T = 8$. The timestep chosen is $\Delta t = \Delta t^*/5$. Fig. 3 shows the error in the position density $\int |\psi| dx$ at all intermediate times. We can see that the magnitude of the error is of $O(10^{-11})$. Note that since the potential is constant, the Taylor expansion approximations for the eikonals and amplitudes are actually exact; see the appendix for further details. These numerical errors may simply come from numerical quadratures in numerical integrals. These results are similar to those in [24].

4.1.2. Interaction of two Gaussians

We demonstrates how two free Gaussian pulses ($V \equiv 0$) move towards each other and interact when they coincide. In this case we are considering $V(x) = 0$ with $\hbar = 2^{-17}$ for $T = 10$ and $N = 2^{17}$. The timestep chosen here is $\Delta t = \Delta t^*/5$ and the initial condition is chosen to be

$$\psi(x, 0) = \psi_+(x, 0) + \psi_-(x, 0),$$

where

$$\psi_+(x, 0) = \frac{1}{\sqrt{\sqrt{\pi}d^2}} \exp\left(-\frac{(x - x_+)^2}{2d^2}\right) \exp\left(\frac{ixp_+}{\hbar}\right)$$

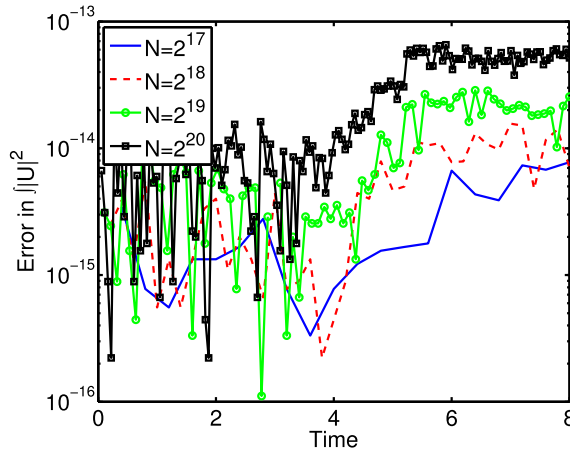


Fig. 3. (Section 4.1.1) Numerical error in $\int |\psi|^2 dx$ in time using $N = 2^{17}$ to 2^{20} .

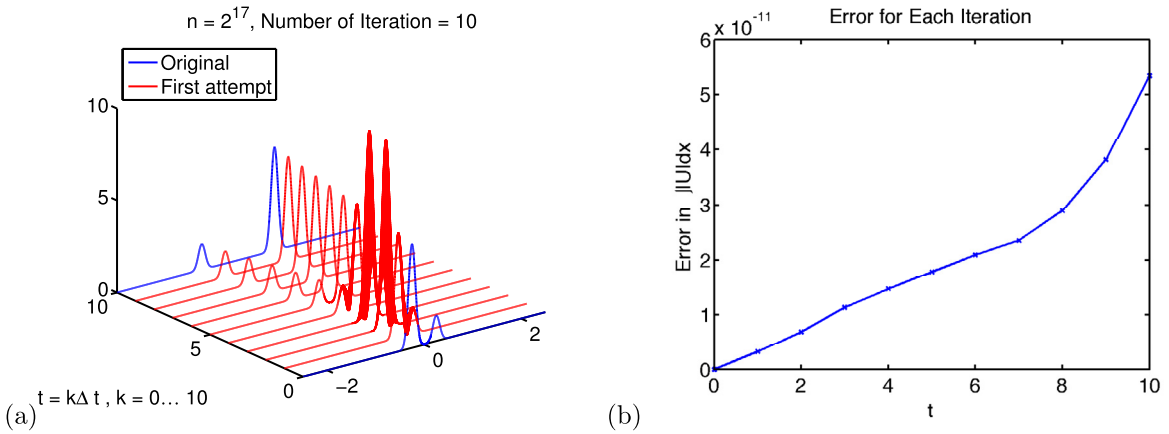


Fig. 4. (Section 4.1.2) (a) Solutions at $t = k\Delta t$ with $k = 0, 1, \dots, 10$. The solution obtained in the first two iterations using the fast Huygens sweeping method are plotted in blue. (b) Error in $\int |U|^2 dx$. (For interpretation of the references to color in this figure legend, the reader is referred to the web version of this article.)

$$\psi_-(x, 0) = \frac{0.5}{\sqrt{\pi d^2}} \exp\left(-\frac{(x - x_+)^2}{2d^2}\right) \exp\left(\frac{ixp_-}{\hbar}\right)$$

and $p_{\pm} = \pm 0.1$, $x_{\pm} = \pm 0.25$, and $d = 0.1$.

Fig. 4(a) shows the solutions at $t = 0, 1, \dots, 10$. Comparing to the original approach which gives solutions only at $t = 5$ immediately, we can now see the solution profile of the wave function ψ at the time when the two Gaussians collide. Fig. 4(b) shows the corresponding error in $\int |\psi|^2 dx$ at each t . The reference solution for this case is exact and we can see that the order of the error is of 10^{-11} which show similar behavior as in Example 4.1.1.

4.1.3. Single Gaussian in the cosine-quadratic potential

We consider the non-trivial potential $V(x) = \frac{1}{8} \cos(2\pi x) + \frac{x^2}{2}$ with $\hbar = 1/256\pi$ and we would like to obtain the numerical solution at the final time $T = 2$ using the time step $\Delta t = \Delta t^*/4$. The initial condition is chosen to be

$$\psi(x, 0) = \frac{1}{\sqrt{\sigma} \sqrt{2\pi}} \exp\left(-\frac{x^2}{4\sigma^2}\right)$$

with $\sigma = 0.1$. Fig. 5 shows the solution at the final time using different mesh points.

Since the potential is non-constant, the analysis in the appendix shows that the Taylor expansion approximation is not exact. Because the error from the forward marching and the backward marching accumulate, the overall numerical error in the final solution using Algorithm 3.1.1 is larger than those obtained as demonstrated in [24]. Nevertheless, as we increase N , the numerical solution does converge to the reference solution, as demonstrated in Fig. 5.

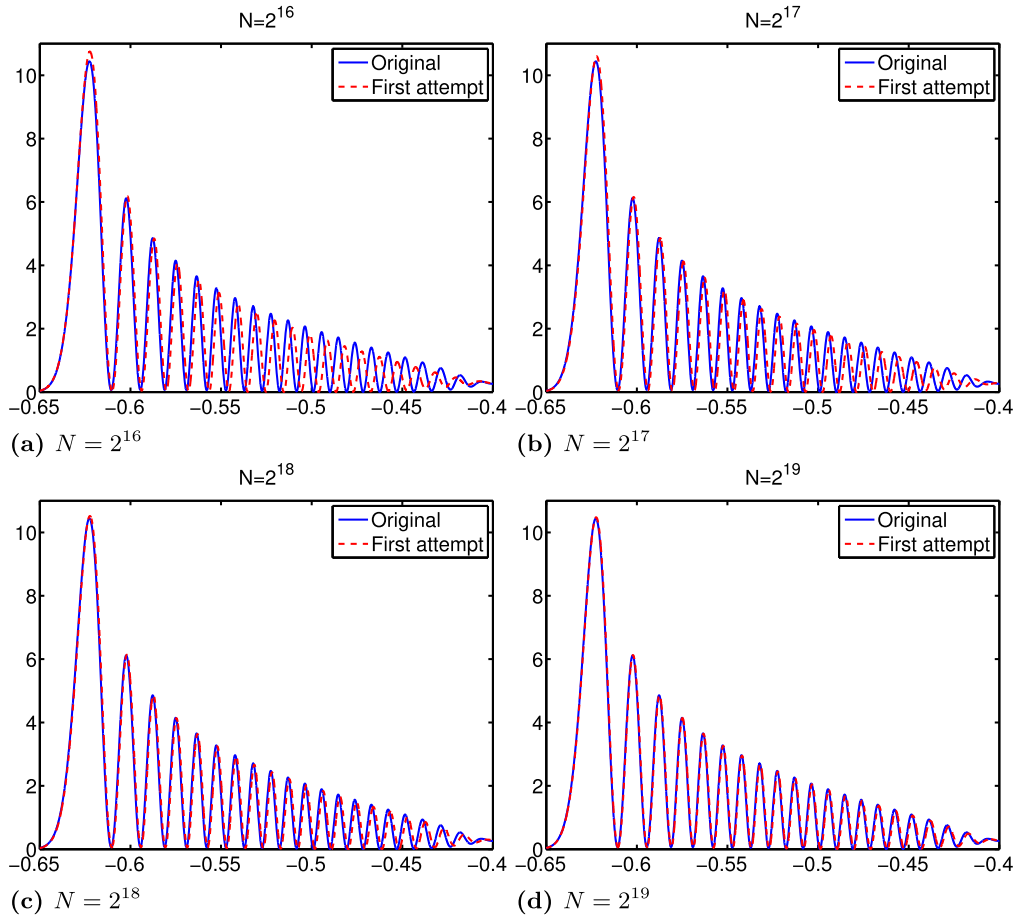


Fig. 5. (Section 4.1.3) Solution computed using Algorithm 3.1.1 (red dashed lines) with different mesh points, together with the reference solution (blue solid lines). (For interpretation of the references to color in this figure legend, the reader is referred to the web version of this article.)

4.1.4. Conservation of energy

In this example, we consider the energy conservation property $\int |U| dx = 1$ as discussed in Theorem 3.1. We consider the non-trivial potential $V(x) = \frac{1}{8} \cos(2\pi x)$ with $h = 1/256\pi$ and we would like to obtain the numerical solution at the final time $T = 8$ using the time step $\Delta t = \Delta t^*/2$. The initial condition is chosen to be

$$\psi(x, 0) = \frac{1}{\sqrt{\sigma} \sqrt{2\pi}} \exp\left(\frac{-x^2}{4\sigma^2}\right)$$

with $\sigma = 0.1$. We compute the error in the solution obtained at each time step using both algorithms as discussed in Section 3.1.1 and Section 3.1.2. For the original Fast Huygens Sweeping algorithm as discussed in Section 2.2, readers are referred to Figure 4.13 in [24]. In Fig. 6b, the error for $N = 2^{20}$ is not illustrated due to insufficient storage capacity.

Figs. 6c and 6d are used to compare the performance of the algorithms in Section 3.1.1 and Section 3.1.2. To make a comparison, we have plotted the errors from the algorithms in Section 3.1.1 and Section 3.1.2 in Fig. 6d. We have in the figure that $\Delta t = \Delta t^*/2$ using the proposed algorithm as discussed in Section 3.1.2 and $\Delta t = \Delta t^*/2, \Delta t^*/4, \Delta t^*/8$ using the algorithm as discussed in Section 3.1.1 with all computations performed with $N = 2^{17}$. We can see that the errors from the algorithm in Section 3.1.1 grows significantly with time. To further compare the errors using the algorithm discussed in Section 3.1.2, Fig. 6c shows errors computed with $\Delta t = \Delta t^*/2, \Delta t^*/4$ and $\Delta t^*/8$. We can see that the errors of solutions computed by Algorithm 3.1.2 are of similar orders with different refinements.

4.2. Two dimensional examples

In this section, we are going to test the proposed algorithms on modeling the propagation of beams in nematic crystals. We denote $Z = \max(z)$ which is similar to the final time in the Schrödinger equation.

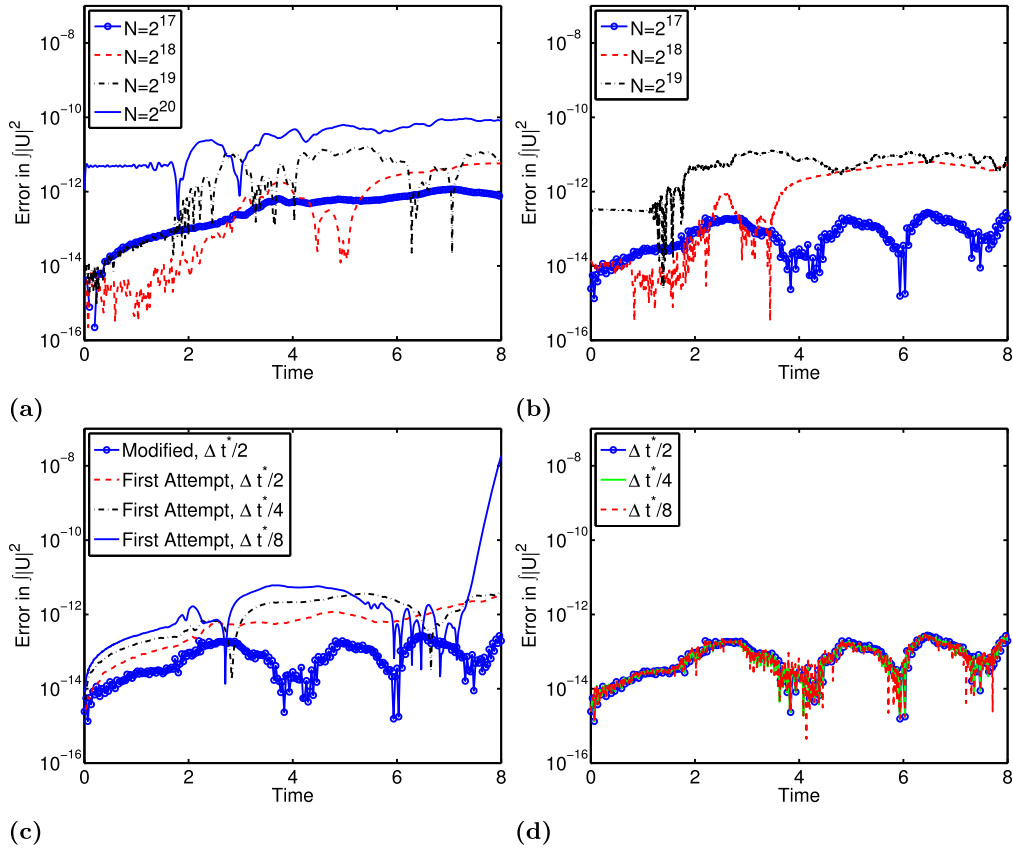


Fig. 6. (Section 4.1.4) Error of the energy conservation property in Example 4.1.4 with various N . (a) Algorithm 3.1.1 and (b) Algorithm 3.1.2. (c) Algorithm 3.1.2 with different refinement and $N = 2^{17}$. (d) Algorithm 3.1.2 and 3.1.1 with different refinement and $N = 2^{17}$.

Table 1

(Section 4.2.1) (a) The computational time $T(A_m, N)$ (in seconds) used for cases of different initial amplitude A_m , the number of mesh points N in solving the parabolic wave equation and (b) the ratios in the computational time.

(a)			
$A_m \setminus N$	2^{16}	2^{17}	2^{18}
3.7	32.9	130.3	558.9
3.75	27.7	105.3	443.2
4	14.1	48.5	187.7
7	10.8	36.2	160.6
9	9.6	39.8	160.0
12	14.1	50.7	185.7

(b)		
$A_m \setminus N$	$T(A_m, 2^{17})/T(A_m, 2^{16})$	$T(A_m, 2^{18})/T(A_m, 2^{17})$
$A_m = 3.7$	3.96112	4.28931
$A_m = 3.75$	3.80606	4.20951
$A_m = 4$	3.44135	3.87294
$A_m = 7$	3.36501	4.43953
$A_m = 9$	4.15228	4.02425
$A_m = 12$	3.58505	3.66626

4.2.1. Single incident beam propagating in the NLC

This example is taken from [27]. We consider a single incident beam with $k = 10000$, $\alpha = 0.1$, $N_x = 2^{18}$, $N_\theta = 513$ and $Z = 10$. The initial condition is chosen to be

$$U(x, 0) = 12 \exp[-(16x)^2]$$

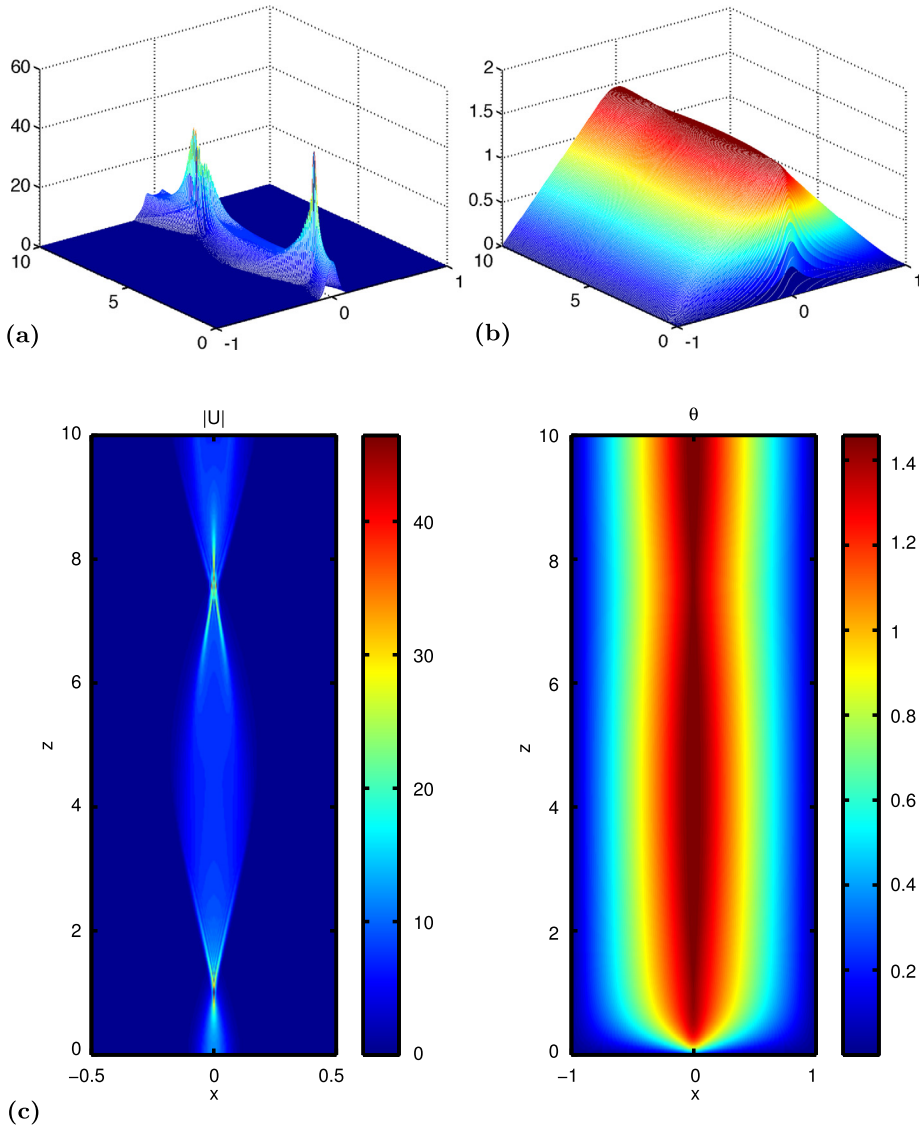


Fig. 7. (Section 4.2.1) Example in [27] with $k = 10000, \alpha = 0.1, N_x = 2^{18}, N_\theta = 257, T = 10, U(x, 0) = 12 \exp[-(16x)^2]$.

which is a single Gaussian profile centered at the origin. Fig. 7 shows the numerical solution obtained by our proposed algorithm. We observe the effects of self-focusing at around $z = 7.5$ (with $k = 10000$ and the initial amplitude $A_m = 12$). It is known that this effect is due to the reorientation of the NLC rod-like molecules (change in θ) [5,2,10,14,35]. In the following examples, we will vary the initial amplitudes A_m , frequency k , number of beams, color and position using the proposed algorithm. The computational time for example in [27] is given by Table 1. Although we cannot prove the computational complexity for the whole algorithm due to the complicated procedures, we can look at the computational time numerically. From Table 1, we see that the ratios N_3/N_2 and N_2/N_1 are approximately 4. This suggests numerically that the computational complexity of the whole procedure is approximately $\mathcal{O}(N^2)$.

For the elliptic equation (2), we have also computed the solution using the Newton’s method. Although the solution converges with fewer iterations, it might converge to a physically irrelevant one. The solution profiles using the Newton’s method are shown in Fig. 8 as a comparison. We found that this solution is not usually observed in physical experiments.

4.2.2. Single incident beam propagating in the NLC in a larger domain using the Algorithm in Section 2.2

Varying the initial amplitude Because of the efficiency in the algorithm, we are now able to study the large z interaction of the beam with the nematic crystal. Here we follow [27] and carefully study the behavior of the solution as we modify the initial amplitude. The parameters are chosen to be the same as those in Fig. 7 but with different initial amplitudes. The choice of the initial amplitudes A_m is the same as that in [27] for easier comparison. We have then obtained the same

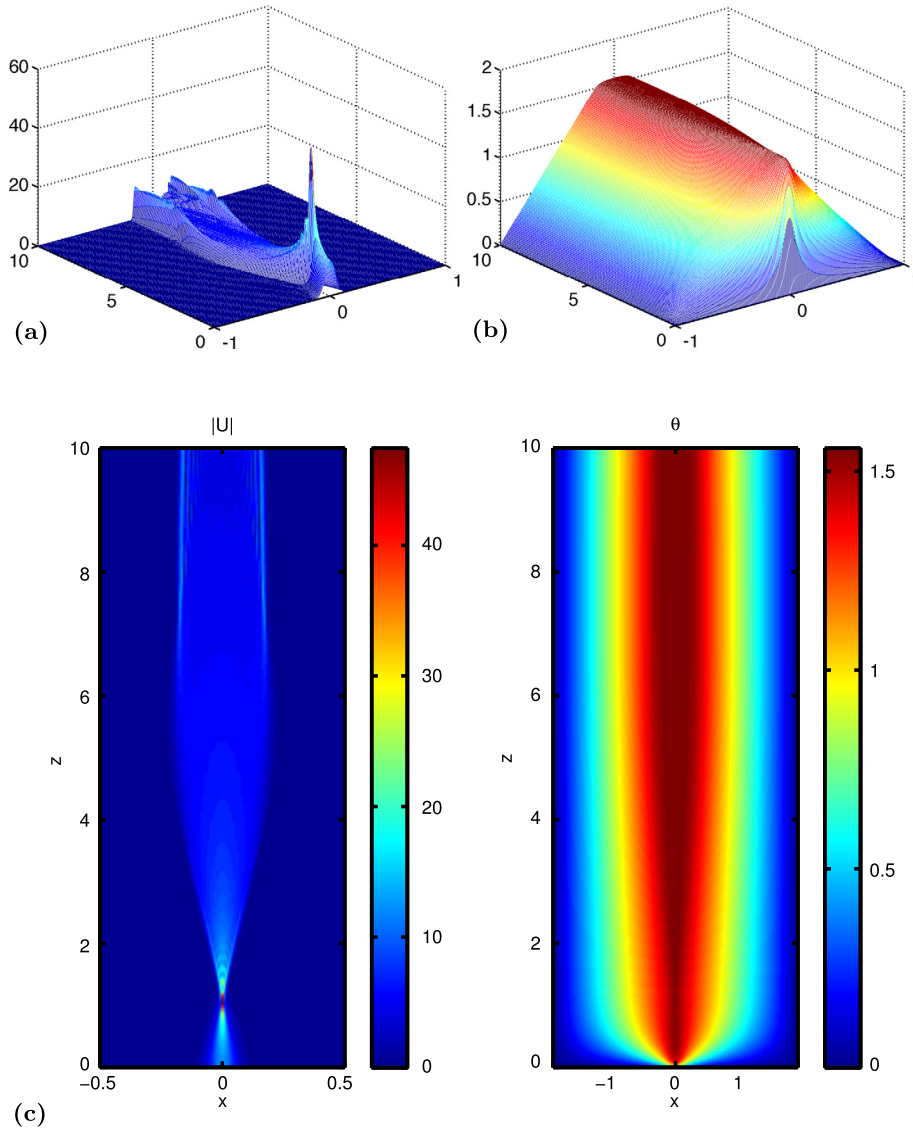


Fig. 8. (Section 4.2.1) Example in [27] with $k = 10000$, $\alpha = 0.1$, $N_x = 2^{18}$, $N_\theta = 257$, $T = 10$, $U(x, 0) = 12 \exp[-(16x)^2]$ using Newton's method. (a) Numerical results of $|U|$ in (1) using Newton's method. (b) Numerical results of θ in (2) using Newton's method. (c) Numerical results of θ in (1) and (2) using Newton's method.

solution profile as that in [27] when using the ADE method for computing the elliptic equation (2). We obtain the solution in $(x, z) \in [-1, 1] \times [0, 30]$ and the initial amplitudes $A_m = 3, 5, 9, 11, 16$, and 20. The initial condition is chosen to be

$$U(x, 0) = A_m \exp[-(16x)^2],$$

which is a single Gaussian profile centered at the origin with a desired amplitude A_m .

Fig. 9 shows the numerical solution from different A_m . We see that the separating distance between the focal spots and the intensity magnitude of the focal spots are increased with respect to the initial amplitude of the beam.

In order to have a distorted state of a nematic liquid crystal, intensity must be higher than the critical value of the total intensity. The directors of the nematic liquid crystal cells are distorted through a supercritical bifurcation. This bifurcation is called the *Frederiks (Fréedericksz) transition* which is a characteristic feature of nematic optics. Beyond this transition, one can easily identify three stages in developing the distorted structure: (i) a distinctive narrowing of the beam by forming focal spots, (ii) an off-axis wandering of the beam by the so-called undulation, and (iii) a break-up into a multiple-beam structure leading to the filamentation [26]. Mathematically, this *Frederiks transition* is known to occur at $I = 1$ with

$$I = \int |U(x, z=0)|^2 dx = \frac{A_m^2}{16} \sqrt{\frac{\pi}{2}}, \quad (16)$$

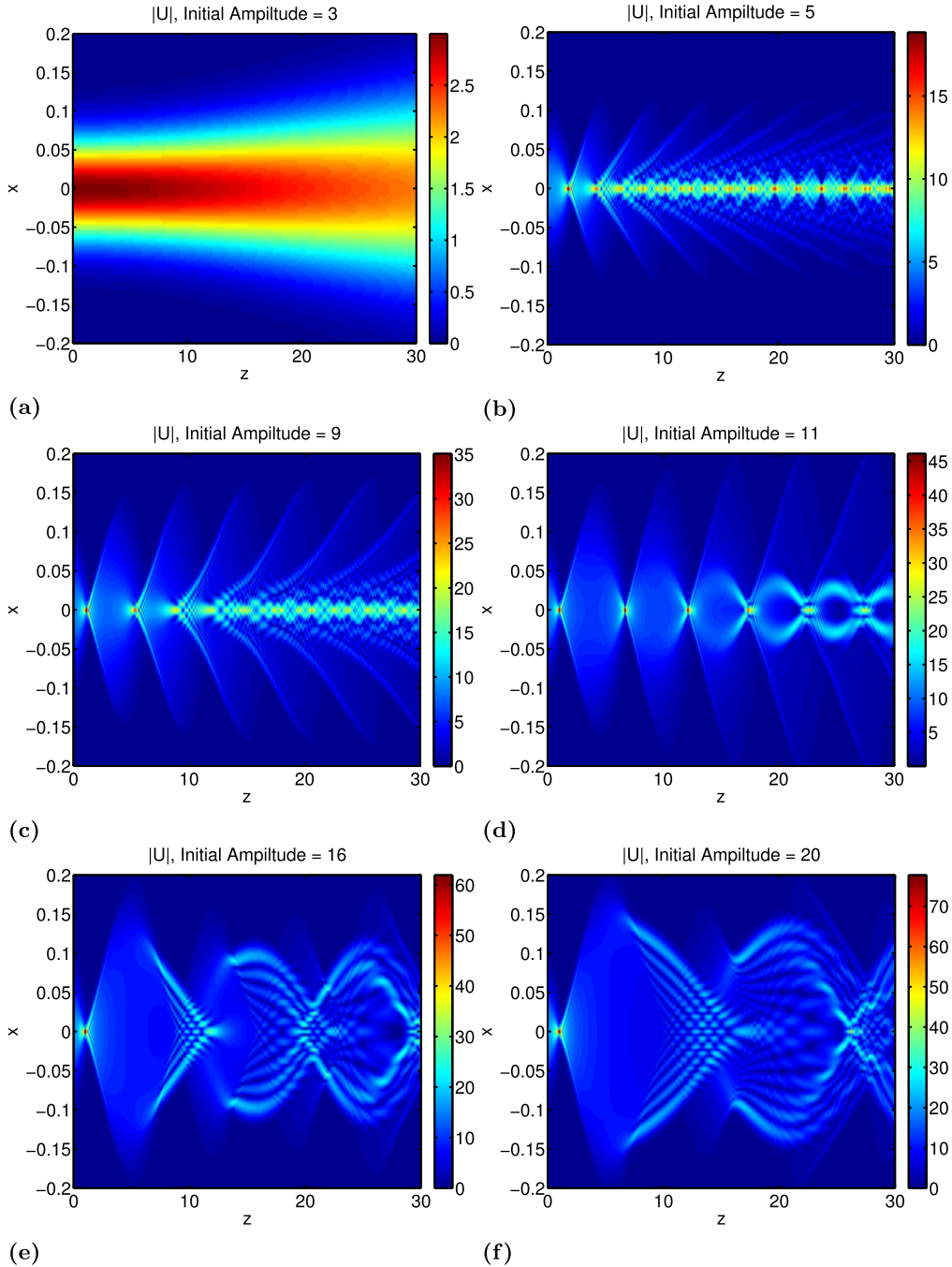


Fig. 9. (Section 4.2.2) Zoom-in solutions of Self-focusing in one optical beam with different initial amplitudes (A_m), where $k = 10000, \alpha = 0.1, N_x = 2^{18}, N_\theta = 513, Z = 30$ and $U(x, 0) = A_m \exp[-(16x)^2]$.

where I is the total intensity of the beam for the incoming beam [27]. These theoretical results are evaluated by imposing an ideal situation of the electric field $U = I\delta(x)$ which is independent of the longitudinal direction z [26]. With such assumptions, the nematic equation becomes a boundary value ODE and yields an estimate

$$\theta^\pm(x) = \max(\theta)(1 \mp x),$$

where the $+$ and $-$ sign denote x in the domains $[0, 1]$ and $[-1, 0]$, respectively, and $\max(\theta)$ satisfies

$$I = \frac{2 \max(\theta)}{\sin 2 \max(\theta)} \geq 1, \tag{17}$$

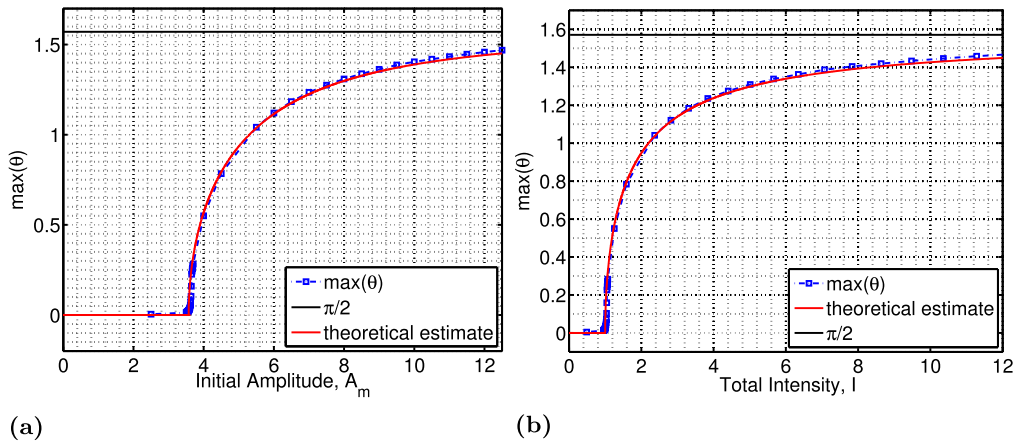


Fig. 10. (Section 4.2.2) (a) $\max(\theta)$ versus the initial amplitude A_m of the beam. (b) $\max(\theta)$ versus the total intensity I given by (16) of the beam where $\alpha = 0.1$, $N_x = 2^{18}$, $N_\theta = 513$, $T = 10$, $U(x, 0) = A_m \exp[-(16x)^2]$.

for the distortion of θ to take place. In the numerical experiments, it is shown that the phenomenon of self-focusing only occurs when the initial amplitude of the optical beam exceeds a certain value. This value is somewhere between 3.5 and 4. In fact, $I \approx 1.07$ ($A_m \approx 3.7$) according to [27] which agrees with our results as shown in Fig. 10a. The theoretical estimate in Fig. 10 is calculated using both (16) and (17). Fig. 10b is the bifurcation diagram in [26] based on both the numerical and theoretical results. Fig. 10 indicates that $\theta = \frac{\pi}{2}$ is the upper bound of θ .

Varying the wave number In this example, we compare the numerical solution using the initial condition

$$U(x, 0) = A_m \exp[-(16x)^2]$$

with a fixed initial amplitude $A_m = 12$ in the computational domain $(x, z) \in [-1, 1] \times [0, 30]$ with $\alpha = 0.1$, $N_x = 2^{18}$ and $N_\theta = 513$. We seek the change in the behavior of the solution as we increase the wave number k ranging from 15000 to 50000. The numerical solutions are shown in Fig. 11. We have the following observations.

Observation 4.1. *The separating distances between the focal spots approximately stay the same with respect to the increase in the wave number.*

Observation 4.2. *As we increase the wave number, the resolution in the solution reduces.*

Observation 4.2 is due to the lower bound (10) because of the increase of k (i.e. smaller \hbar). A hyperbolic secant function is chosen in [36,37]. The original Fast Huygen Sweeping algorithm as discussed in Section 2.2 can also be used for this case and the resulting solution is different from that of using an initial Gaussian profile but a similar conclusion can be drawn. See [36,37] for further details and we do not illustrate the solutions here. An improved scheme is proposed to compute the solution U at those z within the lower bounds and thereby increase the resolution. We will further investigate this property in Section 4.2.3.

Fig. 11 shows the converged solutions of $|U|$ with the initial Gaussian profile. In Fig. 11, we can observe that the separating distances between the focal spots approximately stay the same with respect to the increase in the wave number. The time step that we have chosen to compute for the parabolic equation using the original Fast Huygens Sweeping Algorithm as discussed in Section 2.2 is the one that just exceeds the lower bound Δt^* and is divisible by an integer Z . We can see from the plots that the resolution of the solution getting lower and lower due to the lower bound (10) because of the increase of k (i.e. decrease in \hbar).

4.2.3. Numerical solutions by the proposed numerical scheme

In the examples mentioned, we are using the original Fast Huygen Sweeping algorithm as discussed in Section 2.2 to compute the numerical solutions. The numerical scheme for the parabolic equation is the original Fast Huygens Sweeping algorithm as discussed in Section 2.2 and that for the elliptic equation is the ADE method. As mentioned before, (10) gives a lower bound in Δt when using the original Fast Huygens Sweeping algorithm as discussed in Section 2.2. This means that the solution profiles at z within the interval are not available. Therefore we proposed Algorithm 3.1.2 to tackle the problem. In this section, the original Fast Huygens Sweeping algorithm as discussed in Section 2.2 is used to solve the coupled PDE system. In Fig. 11 and figures in [27], the resolution of the solutions is low because of the limited number of mesh points in the z direction. We attempt to fill the gap between the original mesh points using the original Fast Huygens Sweeping algorithm as discussed in Section 2.2. (See Fig. 2.)

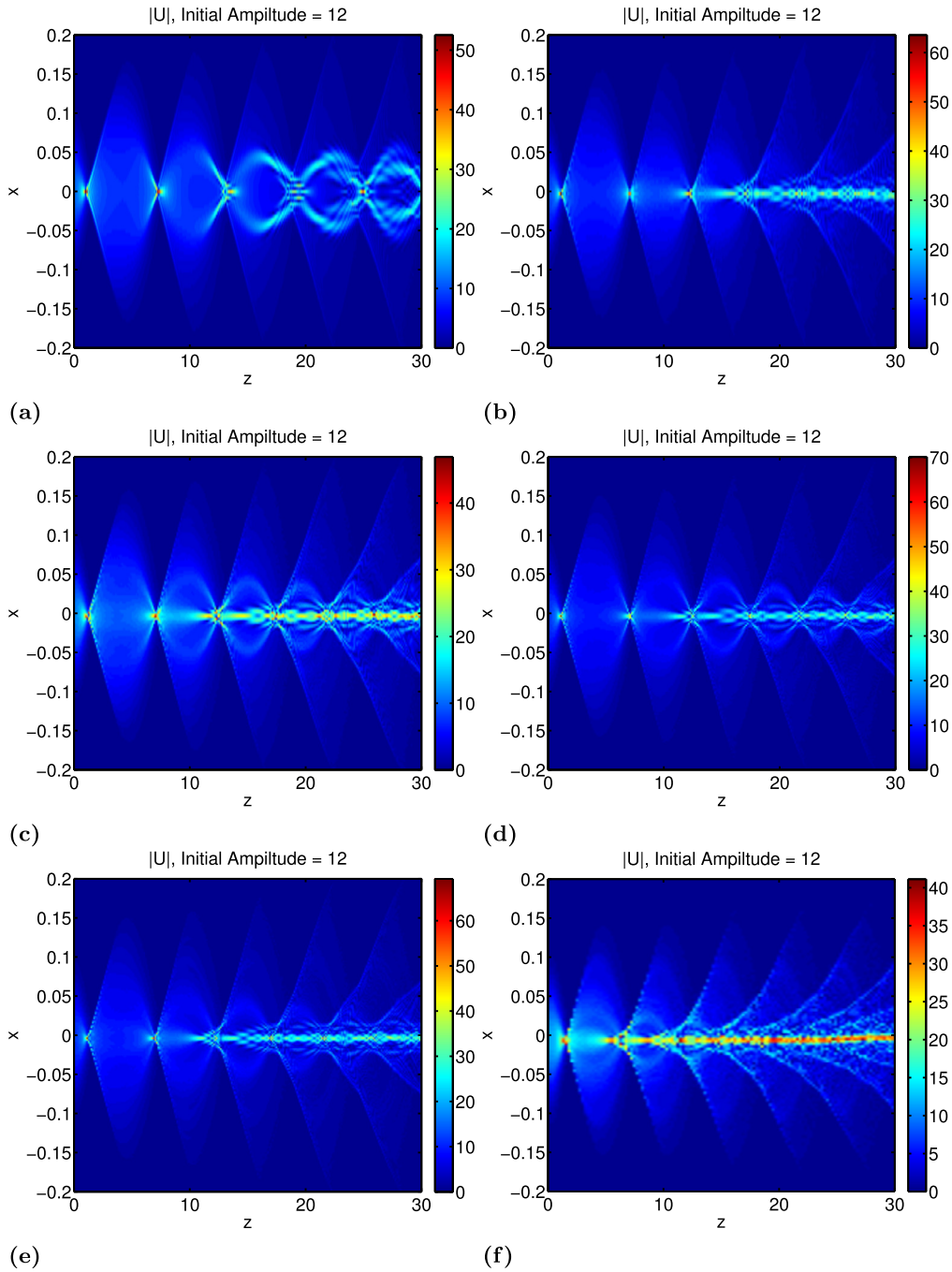


Fig. 11. (Section 4.2.2) Zoom-in solutions of Self-focusing in one optical beam with different initial wave numbers k , where $\alpha = 0.1$, $N_x = 2^{18}$, $N_\theta = 513$, $Z = 30$ and the initial condition $U(x, 0) = 12 \exp[-(16x)^2]$. (a) to (f): $k = 15000, 25000, 35000, 40000, 45000$ and 50000 , respectively.

Improvement in a small computational domain In this section, we follow the results shown in figures in [27]. Algorithm 3.1.2 is used to fill the solution gap within the lower bound for z and $\Delta t = \Delta t^*/4$. Fig. 12 shows the converged solutions $|U|$ for different initial amplitudes for the beam $A_m = 3.7, 3.75, 4, 7, 9, 12$. The parameters are $\alpha = 0.1$, $N_x = 2^{18}$, $N_\theta = 513$ for $A_m = 12$ and $N_\theta = 257$ for the other A_m 's, $k = 10000$, $Z = 10$. One can also tune the maximum number of sweeps in each iteration of the ADE method (chosen to be 100 here). The initial condition is chosen to be

$$U(x, 0) = A_m \exp[-(16x)^2],$$

which is a Gaussian profile centered at the origin.

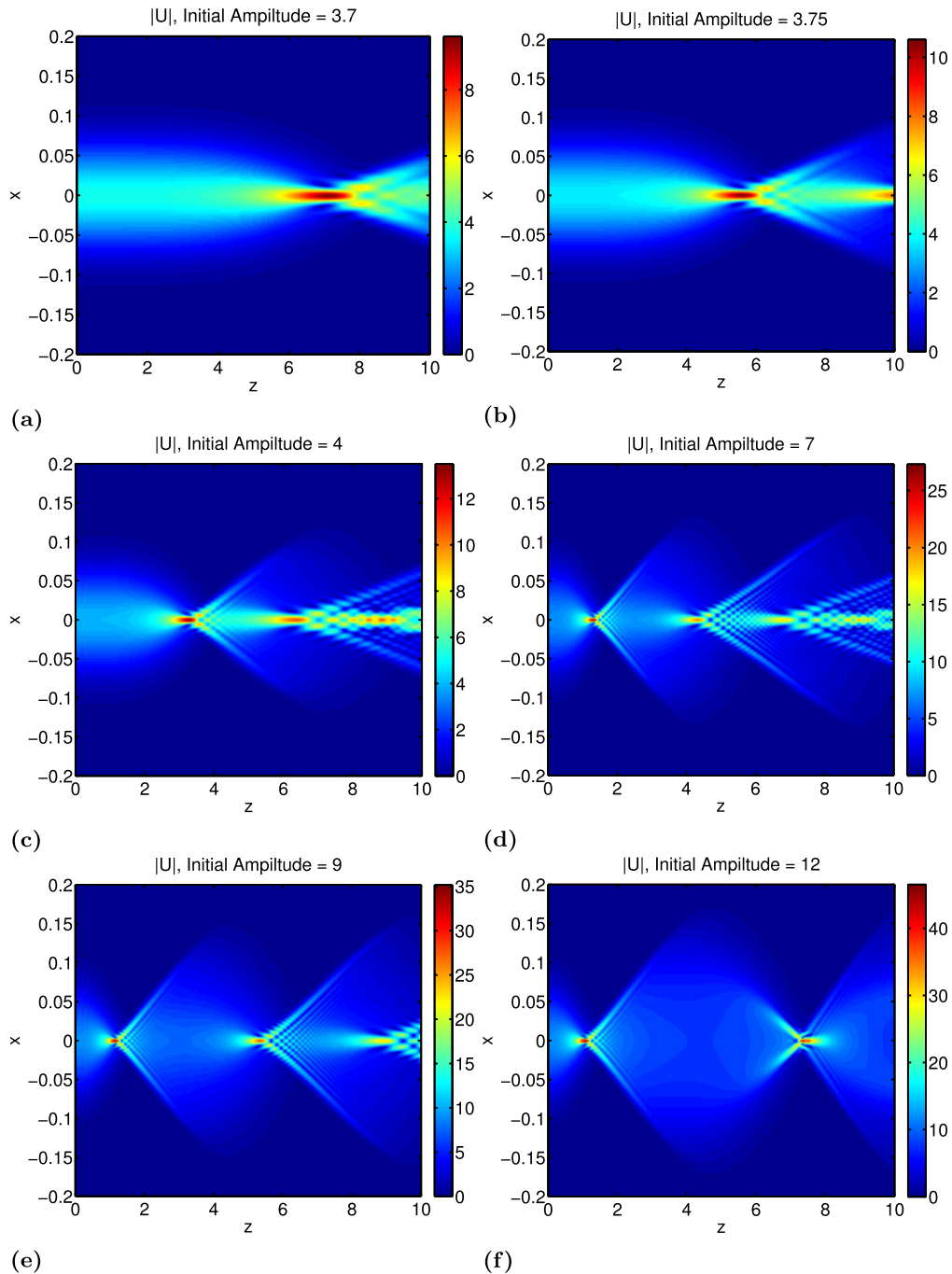


Fig. 12. (Section 4.2.3) Zoom-in solution computed for different initial amplitudes using the proposed scheme with the parameters $\alpha = 0.1$, $N_x = 2^{18}$, $N_\theta = 513$ for $A_m = 12$ and $N_\theta = 257$ for other A_m , $k = 10000$, $Z = 10$, and initial profiles given by $U(x, 0) = A_m \exp[-(16x)^2]$, $\Delta t = \Delta t^*/4$. (a) to (f): $A_m = 3.7, 3.75, 4, 7, 9$ and 12 respectively.

We can see from Fig. 12 that the resolution of the solution profiles indeed increases in comparison to that in figures in [27]. For example, for $A_m = 3.7$, we can observe the tiny oscillations in $|U|$ around the beam center near the focal spot. To have a clearer understanding, we have plotted the longitudinal sections (at $x = 0$) of each solution in Fig. 13.

In Fig. 13, we can observe that the solutions filled by Algorithm 3.1.2 (red dots) matches with the original solution profile using the original Fast Huygens Sweeping algorithm as discussed in Section 2.2 (blue dots). These solutions (red dots) cannot be obtained by interpolation and we will see this in Fig. 14 where we plot the real part of the solution $\text{Re}(U)$ instead of its magnitude $|U|$.

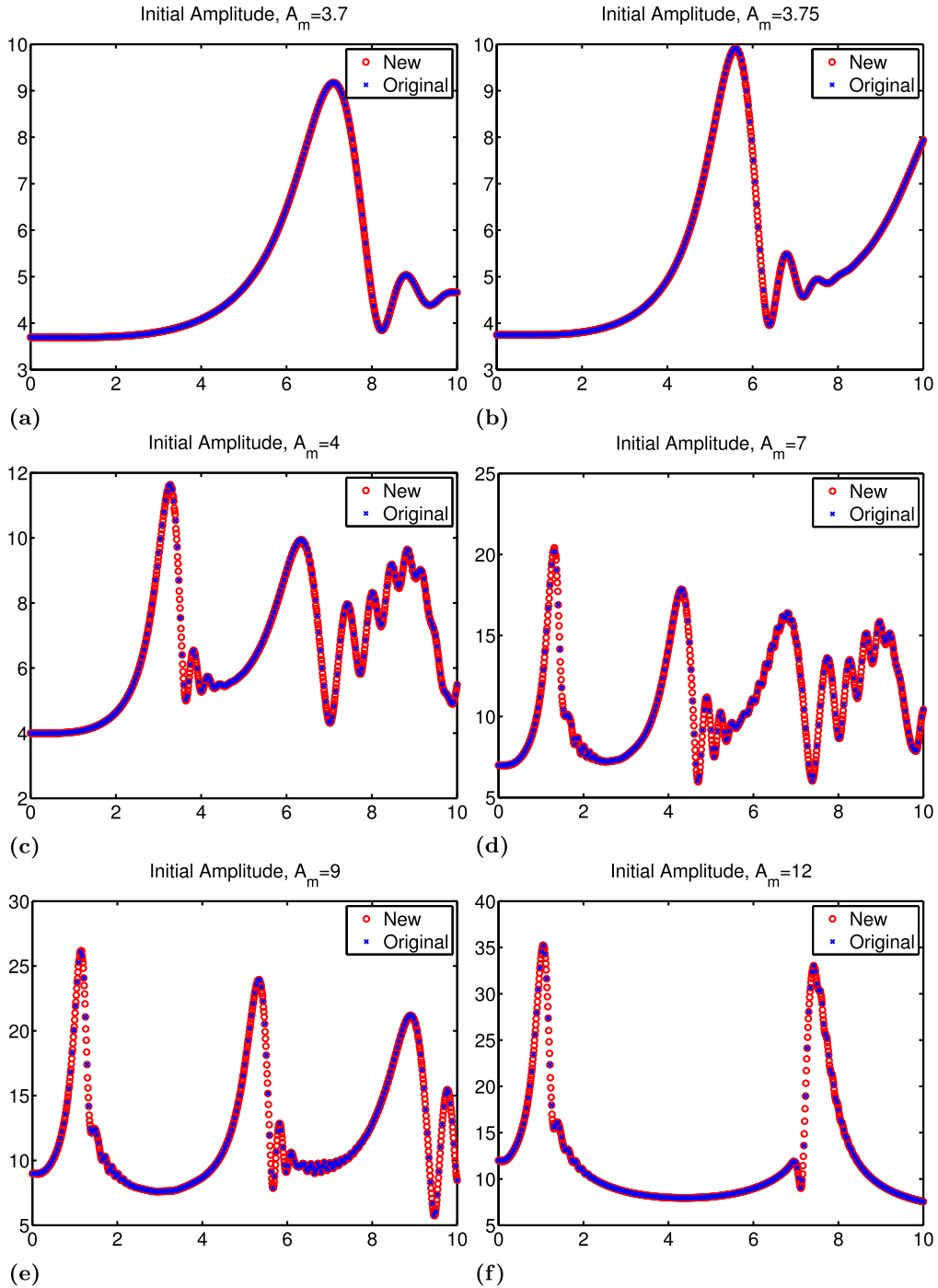


Fig. 13. (Section 4.2.3) Cross sections in Section 4.2.3 for $|U|$ with (a) to (f): $A_m = 3.7, 3.75, 4, 7, 9, 12$ respectively. Blue dots indicate the solutions computed using the original Fast Huygen Sweeping algorithm as discussed in Section 2.2 while red dots are the solutions computed using Algorithm 3.1.2. (For interpretation of the references to color in this figure legend, the reader is referred to the web version of this article.)

By using the gap filling algorithm (Algorithm 3.1.2), we are now able to compute the intermediate solutions which cannot be obtained by simple interpolation because of the observations of the overshooting points.

Errors in the conservation of energy In Fig. 15, we analyze the properties of the conservation of energy mentioned in Section 3.1. Although this property for the fast Huygens sweeping method is unknown for the nonlinear Schrödinger equation, we expect that it may hold for the simple paraxial model when the nonlinear effect is negligible (small A_m). Indeed from Fig. 15 we can see that when A_m increases so that it exceeds the Frederiks transition, the error increases significantly. Since the

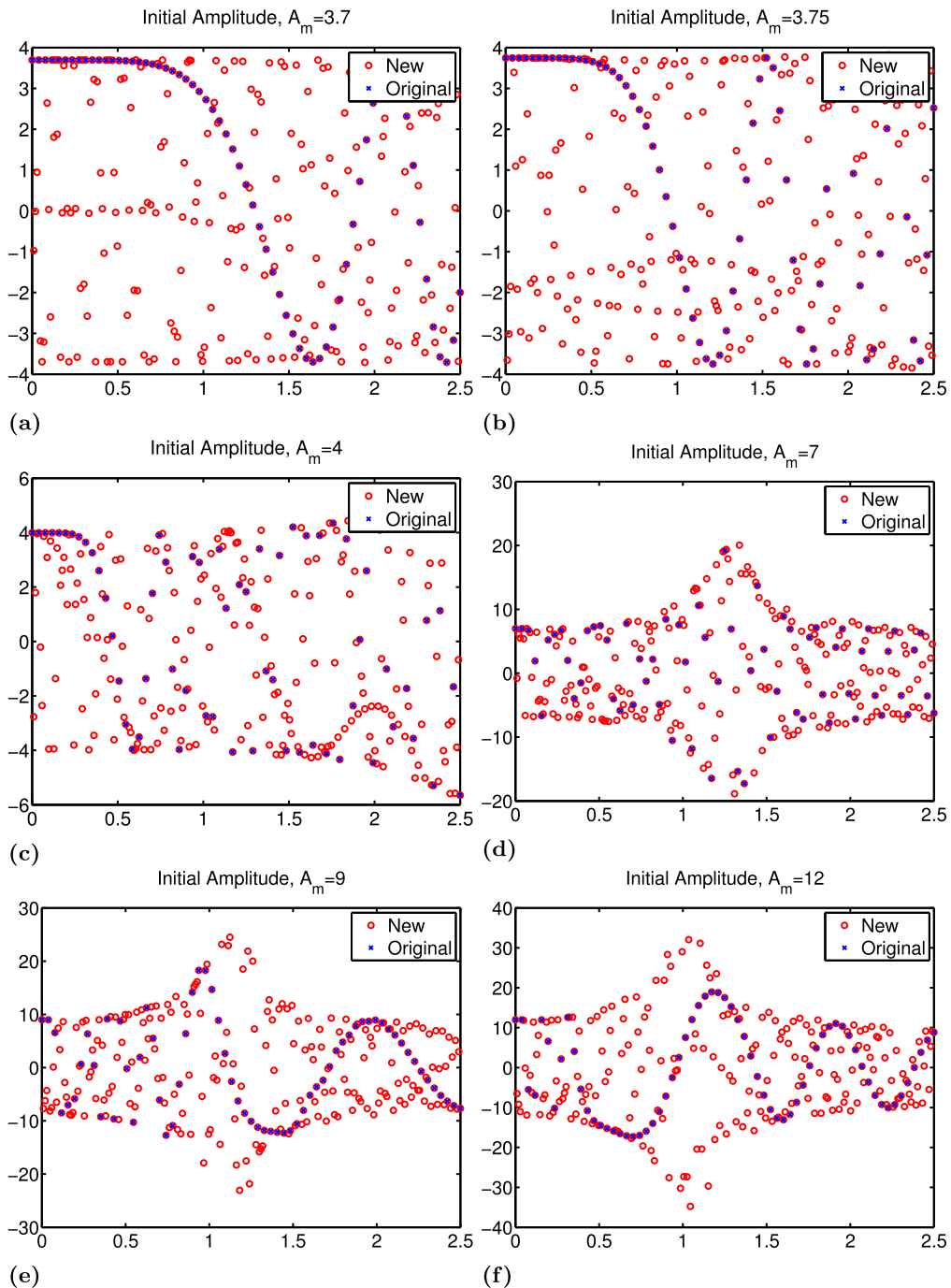


Fig. 14. (Section 4.2.3) Cross sections in Section 4.2.3 for $\text{Re}(U)$ with (a) to (f): $A_m = 3.7, 3.75, 4, 7, 9, 12$ respectively. Blue dots indicate the solutions computed using the original Fast Huygen Sweeping algorithm as discussed in Section 2.2 while red dots are the solutions computed using Algorithm 3.1.2. (For interpretation of the references to color in this figure legend, the reader is referred to the web version of this article.)

self-focusing effect appears when the intensity goes beyond the Frederiks transition, this nonlinear effect of the PDE system increases and the error therefore increases as well.

Numerical experiments on the linear Schrödinger equation has also been done. The error in the energy conservation is found to be negligible for time-dependent potentials. The increase in errors shown in Fig. 15 is due to the nonlinearity in the equation. For a small initial amplitude like $A_m = 3.7$, the error is relatively lower. For the proposed scheme, oscillations are obtained in Fig. 15b which comes from the backward step in (13). As z increases, the error in the original fast Huygens Sweeping algorithm as discussed in Section 2.2 and Algorithm 3.1.2 matches.

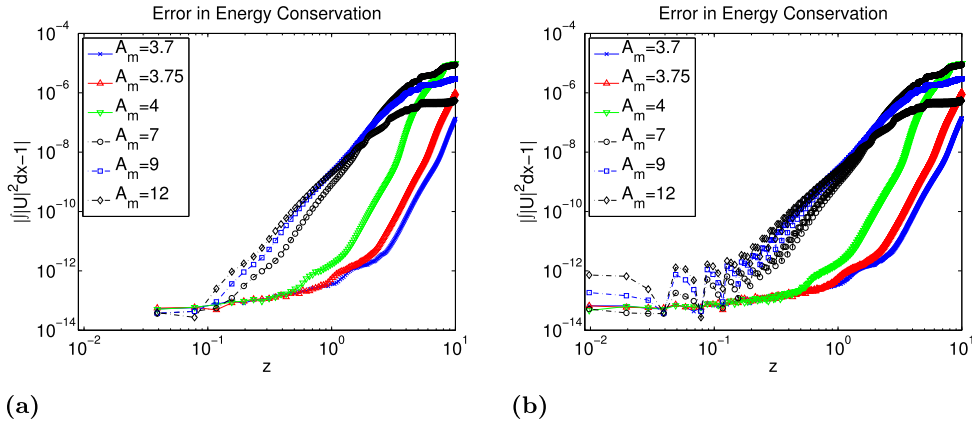


Fig. 15. (Section 4.2.3) Error in the conservation of energy $\int |U|^2 dx$ of (a) Example 4.2.2 using the original fast Huygen Sweeping algorithm as discussed in Section 2.2 and (b) Example 4.2.3 using Algorithm 3.1.2 against z with different initial amplitudes.

Improvement in the case of large wavenumbers k In this section, we follow the results as shown in Fig. 11. Algorithm 3.1.2 is used to fill the solution gap within the lower bound for z and $\Delta t = \Delta t^*/4$. Fig. 16 shows the converged solutions $|U|$ for different wavenumbers k ranging from 15000 to 50000. The parameters chosen are $\alpha = 0.1$, $N_x = 2^{18}$, $N_\theta = 513$, $Z = 30$. One can also tune the maximum number of sweeps in each iteration of the ADE method (chosen to be 200 here). All we need are only the converged steady state solutions. The initial condition is chosen to be

$$U(x, 0) = 12 \exp[-(16x)^2],$$

which is a Gaussian profile centered at the origin.

We can see from Fig. 16 that the resolution of the solution profiles indeed increases compared with that in Fig. 11. To have a clearer understanding, we have plotted the cross section along $x = 0$ of each solution in Fig. 17.

Fredericks transition for the proposed numerical scheme In this section, we follow the analysis in Section 4.2.2 and numerical results are shown for the proposed scheme instead of the original Fast Huygens Sweeping algorithm as discussed in Section 2.2. In Fig. 10, the numerical results matches with the theoretical estimate for $\max(\theta)$. Fredericks Transition occurs at intensity of approximately 1. (See Fig. 18.)

4.2.4. Interaction of incident beams with the same color

In this section, numerical solutions of the simple paraxial model in the computational domain $(x, z) \in [-1, 1] \times [0, 30]$ are computed, where the initial condition is given by two input light beams of the same color. Two examples will be illustrated with the amplitude of the right beam held fixed. The first one is for a smaller intensity (amplitude) and the other one is for a larger intensity (amplitude).

Lower intensity In this example, we have fixed the intensity of the right beam such that $A_m = 3$. Numerical experiments in Section 4.2 show that there is no self-focusing effect for this amplitude in the case of a single beam. And we vary the initial amplitude of the left incident beam. The parameters chosen here are $\alpha = 0.1$, $N_x = 2^{18}$, $k_1 = k_2 = 10000$, $\beta_1 = \beta_2 = 1$ and $N_\theta = 257$. Fig. 19 shows the converged solutions $|U^{(j)}|$ for different amplitudes when the left beam A_m varies from 3 to 12. All we need are only the converged steady state solutions. The initial condition is chosen to be

$$U^{(1)}(x, 0) = A_m \exp[-16^2 (x + 0.25)^2] \text{ and } U^{(2)}(x, 0) = 3 \exp[-16^2 (x - 0.25)^2],$$

which are two Gaussian profiles centered at $x = -0.25$ and $x = 0.25$, respectively.

Higher intensity In this example, we have fixed the intensity of the right beam such that $A_m = 12$. Numerical experiments in Section 4.2 show that there is self-focusing effect for this amplitude in the case of a single beam. And we vary the initial amplitude of the left beam. The parameters chosen here are $\alpha = 0.1$, $N_x = 2^{18}$, $k_1 = k_2 = 10000$, $\beta_1 = \beta_2 = 1$ and $N_\theta = 257$. Fig. 20 shows the converged solutions $|U^{(j)}|$ for different amplitudes when the left beam A_m varies from 3 to 12. All we need are only the converged steady state solutions. The initial condition is chosen to be

$$U^{(1)}(x, 0) = A_m \exp[-16^2 (x + 0.25)^2] \text{ and } U^{(2)}(x, 0) = 4 \exp[-16^2 (x - 0.25)^2],$$

which are two Gaussian profiles centered at $x = -0.25$ and $x = 0.25$, respectively.

We can observe from the numerical results that both beams are mutually affecting each other. When the amplitude or position of one beam varies, the solution profile of the other beam changes.

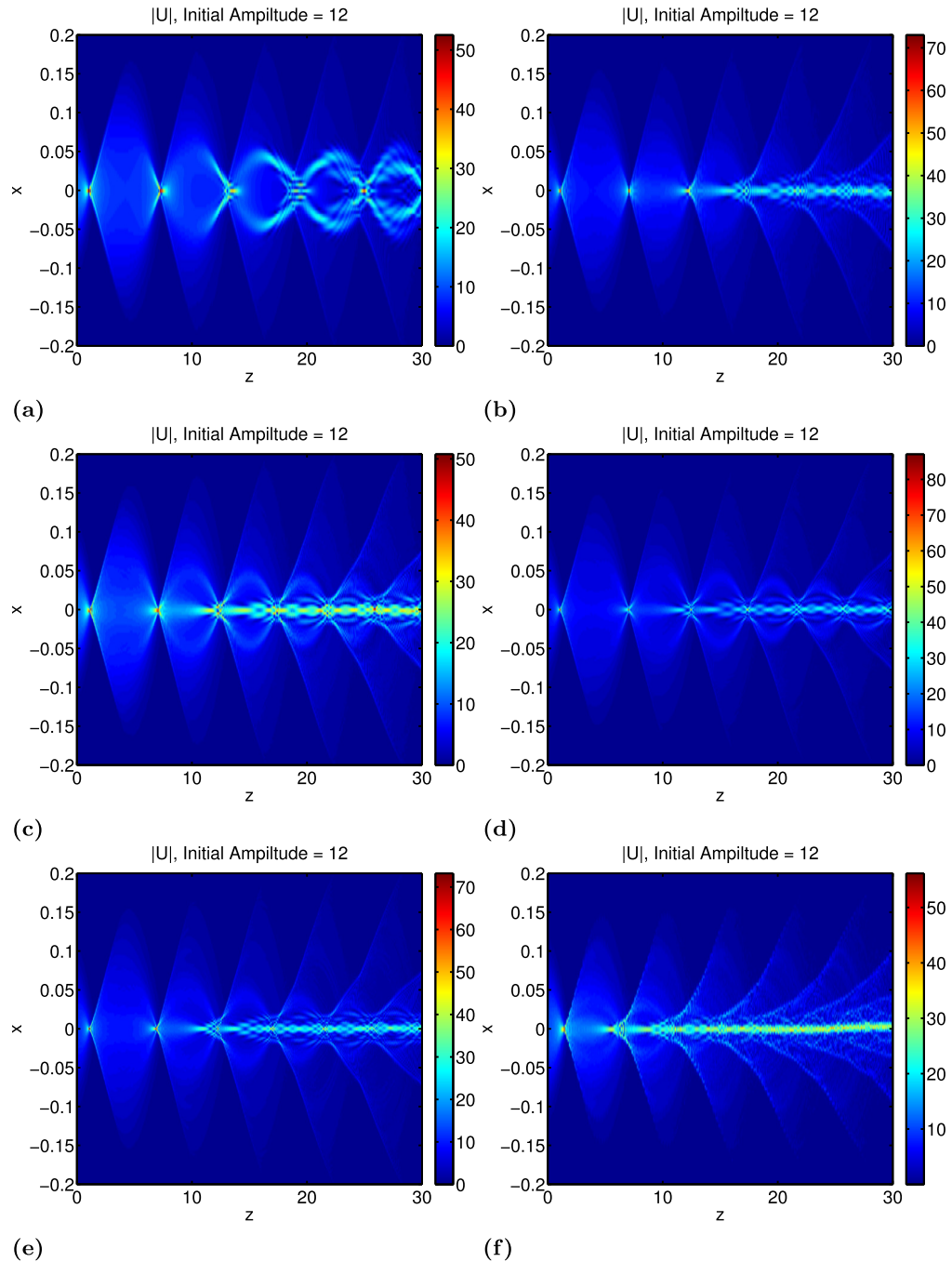


Fig. 16. (Section 4.2.3) Zoom-in solution computed for different wavenumber with the parameters $\alpha = 0.1$, $N_x = 2^{18}$, $N_\theta = 513$, $Z = 30$. The initial profiles are given by $U(x, 0) = 12 \exp[-(16x)^2]$, $\Delta t = \Delta t^*/R$ where $R = \text{floor}(k/10000)$. (a) to (f): $k = 15000, 25000, 35000, 40000$ and 50000 , respectively.

4.2.5. Interaction of incident beams with different colors

We first consider the numerical solutions of the simple paraxial model in the computational domain $(x, z) \in [-1, 1] \times [0, 30]$, where the initial condition is given by two input light beams of different colors. Two examples will be illustrated with the amplitude of the right beam held fixed. The first one is for a smaller intensity (amplitude) and the other one is for a larger intensity (amplitude).

Lower intensity In this example, we have fixed the intensity of the right beam such that $A_m = 3$. Numerical experiments in Section 4.2 show that there is no self-focusing effect for this amplitude in the case of a single beam. And we vary the initial

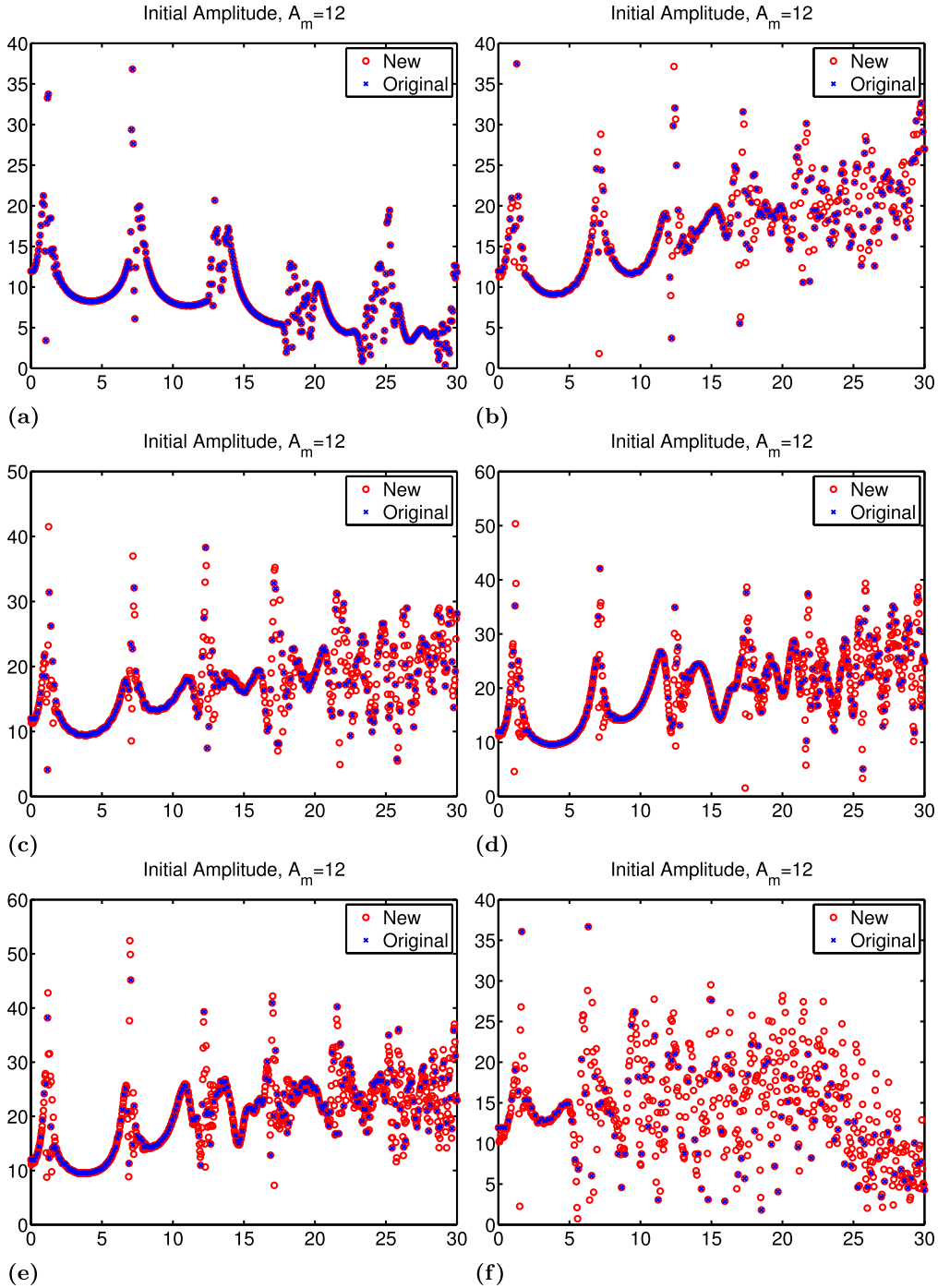


Fig. 17. (Section 4.2.3) Cross sections in Section 4.2.3 with (a) to (f): $k = 15000, 25000, 35000, 40000, 45000$ and 50000 , respectively. Blue dots indicate the solutions computed using the original scheme original Fast Huygen Sweeping algorithm as discussed in Section 2.2 while red dots are the solutions computed using Algorithm 3.1.2. (For interpretation of the references to color in this figure legend, the reader is referred to the web version of this article.)

amplitude of the left incident beam. The parameters chosen here are $\alpha = 0.1, N_x = 2^{18}, k_1 = 10000, k_2 = 8000, \beta_1 = 1, \beta_2 = 0.75$ and $N_\theta = 257$. Fig. 21 shows the converged solutions $|U^{(j)}|$ for different amplitudes when the left beam A_m varies from 3 to 12. All we need are only the converged steady state solutions. The initial condition is chosen to be

$$U^{(1)}(x, 0) = A_m \exp[-16^2 (x + 0.25)^2] \text{ and } U^{(2)}(x, 0) = 3 \exp[-16^2 (x - 0.25)^2],$$

which are two Gaussian profiles centered at $x = -0.25$ and $x = 0.25$, respectively.

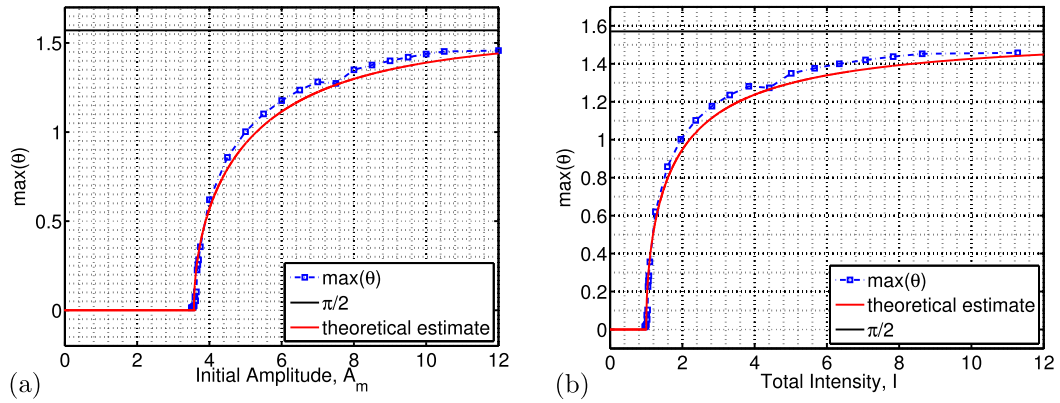


Fig. 18. (Section 4.2.3) (a) $\max(\theta)$ against the initial amplitude A_m of the optical beam. (b) $\max(\theta)$ against total intensity I given by (16) of the optical beam, where $\alpha = 0.1$, $N_x = 2^{18}$, $N_\theta = 513$, $T = 10$, $U(x, 0) = A_m \exp[-(16x)^2]$.

Higher intensity In this example, we have fixed the intensity of the right beam such that $A_m = 4$. Numerical experiments in Section 4.2 show that there is self-focusing effect for this amplitude in the case of a single beam. And we vary the initial amplitude of the left beam. The parameters chosen here are $\alpha = 0.1$, $N_x = 2^{18}$, $k_1 = 10000$, $k_2 = 8000$, $\beta_1 = 1$, $\beta_2 = 0.75$ and $N_\theta = 257$. Fig. 22 shows the converged solutions $|U^{(j)}|$ for different amplitudes for the left beam A_m varies from 3 to 12. All we need are only the converged steady state solutions. The initial condition is chosen to be

$$U^{(1)}(x, 0) = A_m \exp[-16^2(x + 0.25)^2] \text{ and } U^{(2)}(x, 0) = 4 \exp[-16^2(x - 0.25)^2],$$

which are two Gaussian profiles centered at $x = -0.25$ and $x = 0.25$, respectively.

Same intensity with varying position In this example, we have fixed the intensity of both beams such that $A_m = 3$. Examples in the above show that there is no self-focusing effect for this amplitude in the case of a single beam. And we vary the position of the beams. The parameters chosen here are $\alpha = 0.1$, $N_x = 2^{18}$, $k_1 = 10000$, $k_2 = 8000$, $\beta_1 = 1$, $\beta_2 = 0.75$, $Z = 30$ and $N_\theta = 257$. Fig. 23 shows the converged solutions $|U^{(j)}|$ with different centre positions $x = -x_0$ and $x = x_0$, where x_0 varies from 0.03 to 0.19. We are interested in steady state solutions. The initial condition is chosen to be

$$U^{(1)}(x, 0) = 3 \exp[-16^2(x + x_0)^2] \text{ and } U^{(2)}(x, 0) = 3 \exp[-16^2(x - x_0)^2],$$

which are two Gaussian profiles centered at $x = -x_0$ and $x = x_0$, respectively.

4.3. Three dimensional examples

Because of the computational cost, most numerical results are done in two dimensions only. In this section, we demonstrate the efficiency of the proposed scheme for the paraxial model by showing some three dimensional computations with different parameters. Fig. 24 and Fig. 25 show the results of one beam and two beams, respectively, which agree with the observations in the two-dimensional examples.

5. Conclusion

In this paper, we have proposed a new method for simulating the evolution of light beams in nematic liquid crystals as modeled by (1) and (2). It is a coupled PDE system which consists of a parabolic PDE and an elliptic PDE. We follow the Fast Huygens Sweeping method proposed in [24] to solve the parabolic PDE and the Alternating Direction Explicit method [17,4,18] to solve the elliptic PDE. We have followed the original Fast Huygens Sweeping algorithm as discussed in Section 2.2 such that the parabolic PDE can be computed in an efficient way and the elliptic equation can be computed in an unconditionally stable way. Several numerical results have shown that the effect of self-focusing occurs when the amplitude (intensity) exceeds a certain threshold depending on the Fredericks transition. It is observed that the separation distances between focal spots and the number of focal spots increase as the initial amplitude increases. When the wavenumber increases, the locations of the focal spots remain approximately the same. We also observed that the nematic field θ is bounded above by $\pi/2$. We remove the lower bound in the original fast Huygens Sweeping Method as discussed in Section 2.2 by Algorithm 3.1.2. In the case of two beams, both beams will influence each other such that the critical value of Fredericks transition for a single beam is no longer valid. Finally, we have also illustrated the errors in the conservation of energy, and numerical results in two- and three-dimensional spaces demonstrate the efficiency of the overall algorithm.

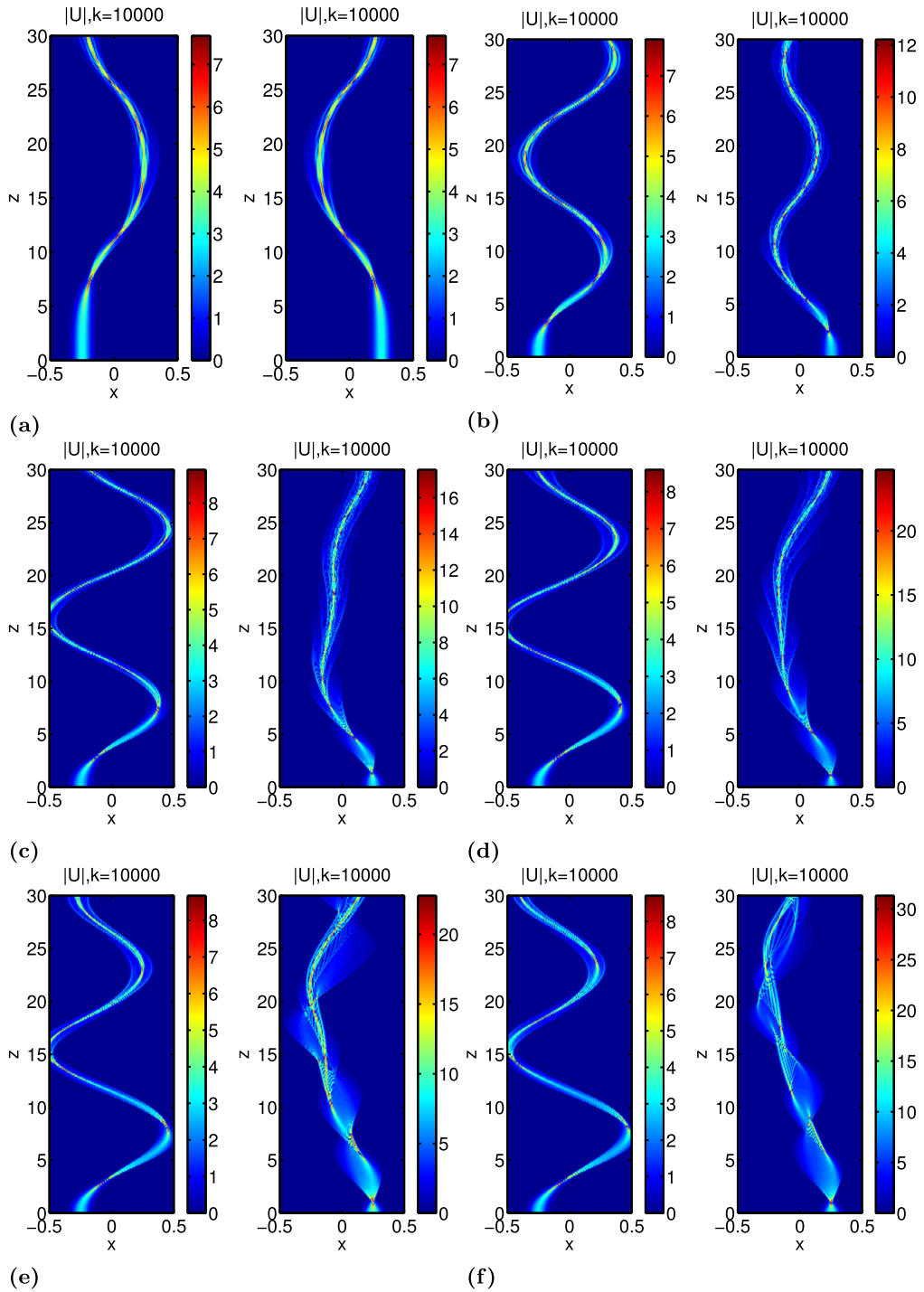


Fig. 19. (Section 4.2.4) Intersection of two-color optical beams with $\alpha = 0.1$, $N_x = 2^{18}$, $k_1 = 10000$, $k_2 = 10000$, $\beta_1 = \beta_2 = 1$, $Z = 30$, and initial profiles given by $U^{(1)}(x, 0) = A_m \exp[-16^2(x + 0.25)^2]$ and $U^{(2)}(x, 0) = 3 \exp[-16^2(x - 0.25)^2]$. (a) Initial conditions for the iterations and (b) converged $|\sum_j U^{(j)}|$ and θ . (a) to (f): $A_m = 3, 4, 6, 8, 10$ and 12 , respectively.

Acknowledgement

The work of Leung was supported in part by the Hong Kong RGC grants 16303114 and 16309316. Qian is partially supported by National Science Foundation (NSF) Grants 1522249 and 1614566.

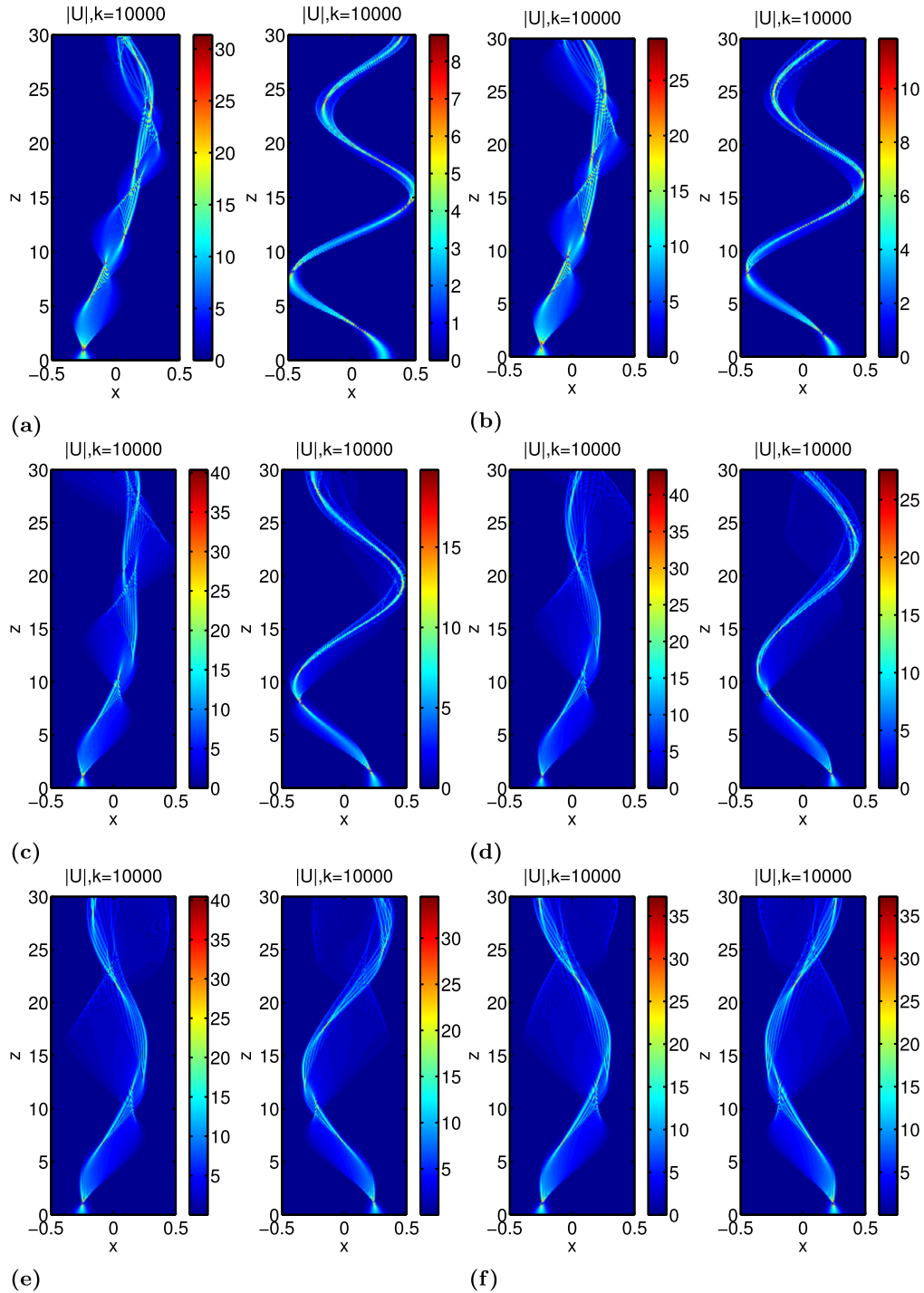


Fig. 20. (Section 4.2.4) Intersection of two-color optical beams with $\alpha = 0.1$, $N_x = 2^{18}$, $k_1 = 10000$, $k_2 = 10000$, $\beta_1 = \beta_2 = 1$, $T = 30$, and initial profiles given by $U^{(1)}(x, 0) = A_m \exp[-16^2(x + 0.25)^2]$ and $U^{(2)}(x, 0) = 12 \exp[-16^2(x - 0.25)^2]$. Converged $|U^{(j)}|$ with varying initial amplitudes of the beams. (a) to (f): $A_m = 3, 4, 6, 8, 10$ and 12 , respectively.

Appendix A. Taylor expansion approximations for the eikonals and amplitudes

In the problem formulation, we have computed the Green's function asymptotically to obtain the semi-classical solution after we substituted the WKBJ ansatz into the Schrödinger equation. Consequently, we have obtained the following set of equations with ξ as the momentum variable used in the convolution integral:

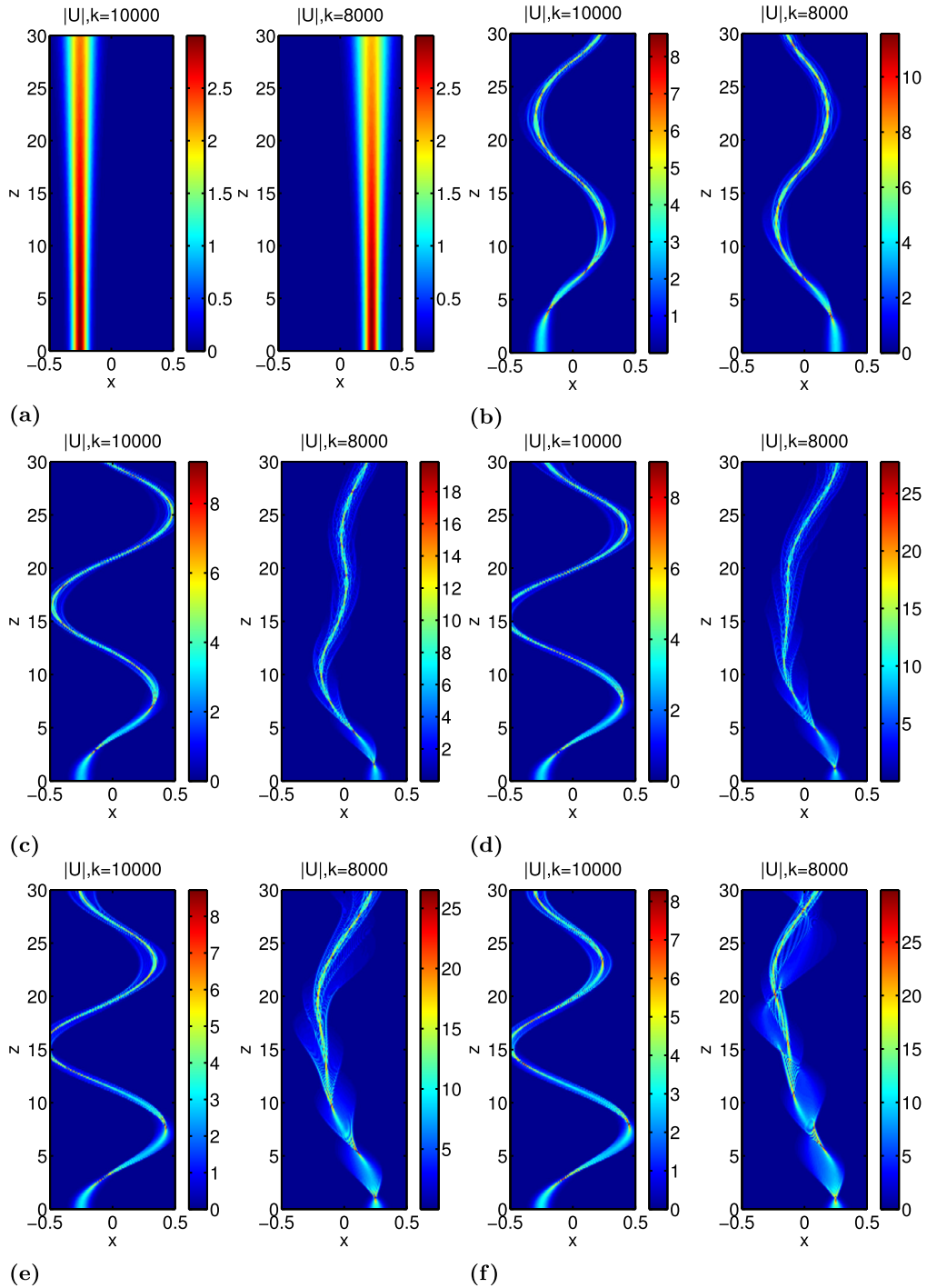


Fig. 21. (Section 4.2.5) Converged $|U^{(j)}|$ for the intersection of two-color optical beams with $\alpha = 0.1$, $N_x = 2^{18}$, $k_1 = 10000$, $k_2 = 8000$, $\beta_1 = 1$, $\beta_2 = 0.75$, $Z = 30$, and initial profiles given by $U^{(1)}(x, 0) = A_m \exp[-16^2(x + 0.25)^2]$ and $U^{(2)}(x, 0) = 3 \exp[-16^2(x - 0.25)^2]$. (a) to (f): $A_m = 3, 4, 6, 8, 10$ and 12 , respectively.

$$\tau_t + V(x) + \frac{1}{2}|\nabla\tau|^2 = 0, \quad t > t_0,$$

$$\tau(x, t_0; \xi) = x \cdot \xi,$$

$$A_t + \nabla\tau \cdot \nabla A + \frac{1}{2}\Delta\tau A = 0, \quad t > t_0,$$

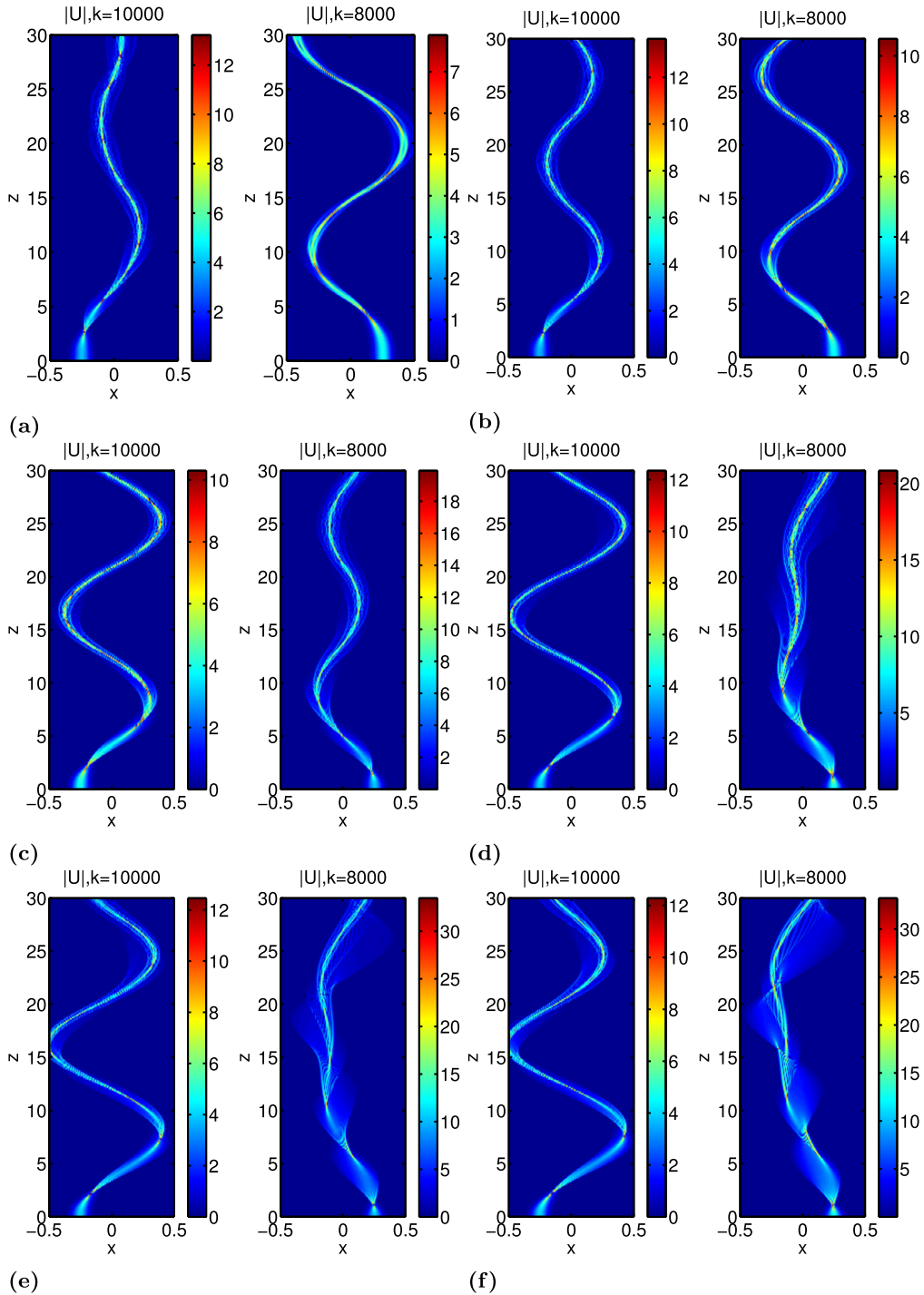


Fig. 22. (Section 4.2.5) Converged $|U^{(j)}|$ for the intersection of two-color optical beams with $\alpha = 0.1$, $N_x = 2^{18}$, $k_1 = 10000$, $k_2 = 8000$, $\beta_1 = 1$, $\beta_2 = 0.75$, $Z = 30$, and initial profiles given by $U^{(1)}(x, 0) = A_m \exp[-16^2(x + 0.25)^2]$ and $U^{(2)}(x, 0) = 4 \exp[-16^2(x - 0.25)^2]$. (a) to (f): $A_m = 3, 4, 6, 8, 10$ and 12 , respectively.

$$A(x, t_0; \xi) = 1 .$$

Then we approximate the amplitude and phase functions using the Taylor expansion so as to obtain analytic formulae for the convolution. To avoid confusion with the Laplacian, we write t instead of Δt here. For small time t , expand both the phase and amplitude functions using the Taylor series in time:

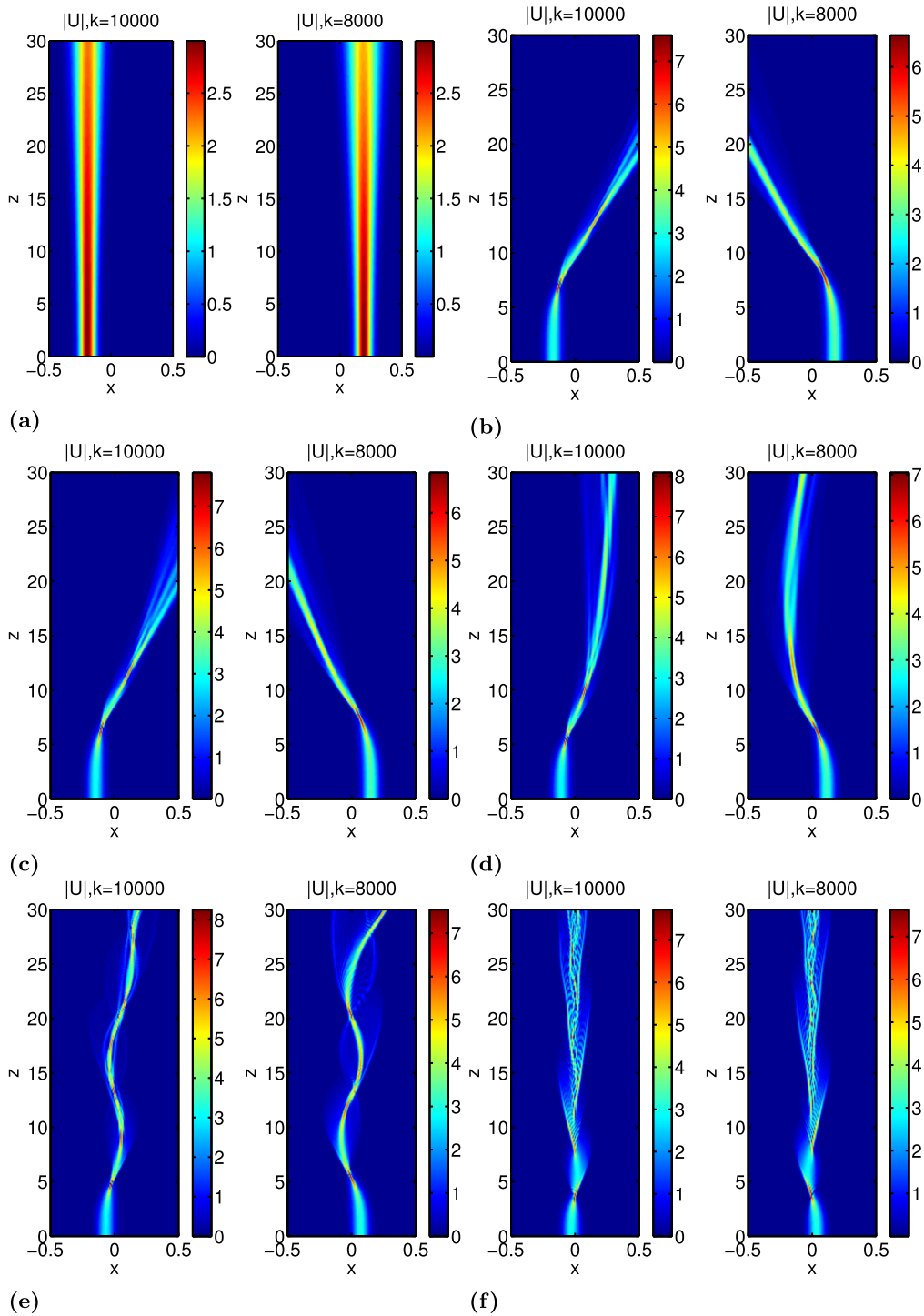


Fig. 23. (Section 4.2.5) Intersection of two-color optical beams with $\alpha = 0.1$, $N_x = 2^{18}$, $k_1 = 10000$, $k_2 = 8000$, $\beta_1 = 1$, $\beta_2 = 0.75$, $Z = 30$, and initial profiles given by $U^{(1)}(x, 0) = 3 \exp[-16^2(x + x_0)^2]$ and $U^{(2)}(x, 0) = 3 \exp[-16^2(x - x_0)^2]$. Converged $|U^{(j)}|$ with varying separation distance between the beams. (a) to (f): $x_0 = 0.19, 0.17, 0.15, 0.11, 0.07$ and 0.03 , respectively.

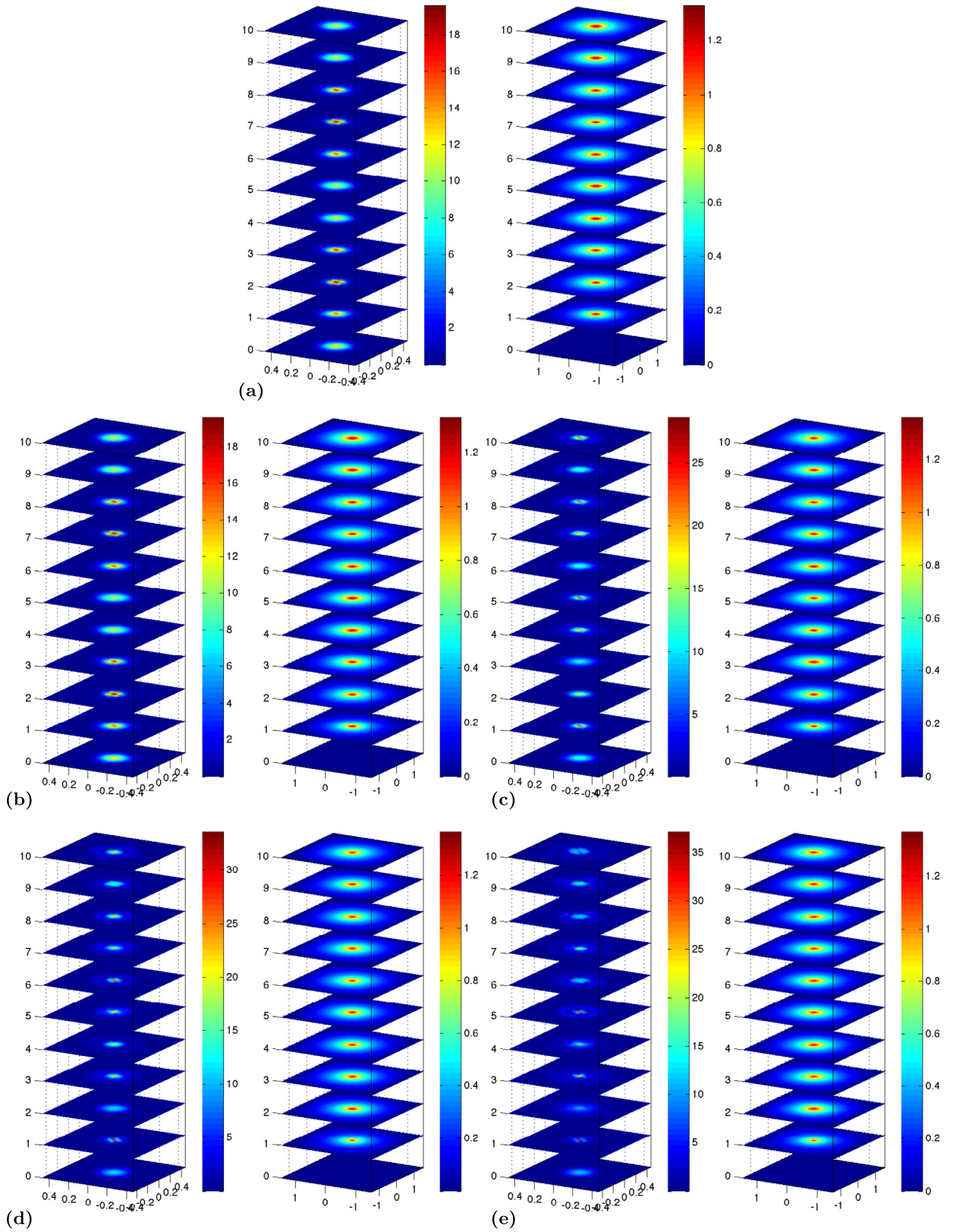


Fig. 24. (Section 4.3) Optical self-focusing in three dimensions with $k = 256$, $N_x = 2^{11}$, $N_\theta = 65$ and initial profile given by $U(x, 0) = 12 \exp[-8^2(x^2 + y^2)]$. (a) Intensity of the incident beam at the initial time when there is no nonlinear effect from the NLC. (b–e) The steady state solutions of the intensity and θ . (b) $\alpha = 0.05$, (c) $\alpha = 0.10$, (d) $\alpha = 0.15$ and (e) $\alpha = 0.20$.

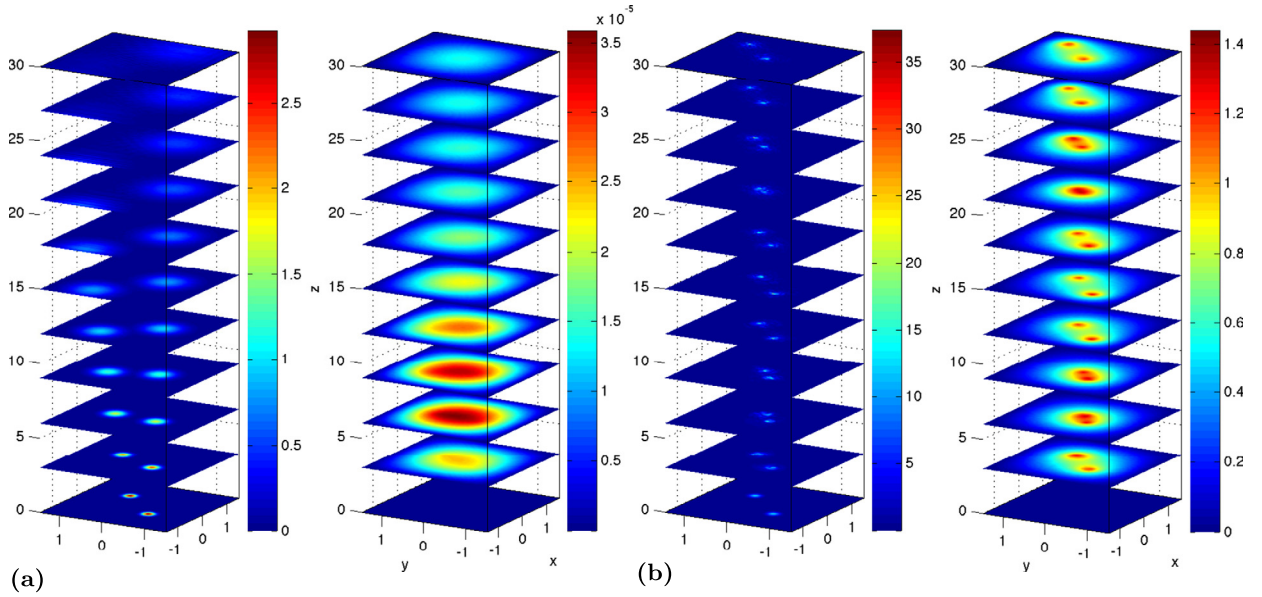


Fig. 25. (Section 4.3) Optical self-focusing of two different frequency beams in three dimensions with $k_1 = 512$, $k_2 = 256$, $N_x = 2^{11}$, $N_\theta = 65$, $\alpha = 0.20$, $\beta_1 = 1$, $\beta_2 = 0.75$ and initial profiles given by $U_1(x, y, 0) = 12 \exp[-8^2((x - 0.5)^2 + (y - 0.5)^2)] \exp(-ik_1x/10)$ and $U_2(x, y, 0) = 12 \exp[-8^2((x + 0.5)^2 + (y + 0.5)^2)] \exp(ik_2x/10)$. (a) Intensity of the incident beam at the initial time when there is no nonlinear effect from the NLC. (b) The steady state solutions of the intensity and θ .

$$\begin{aligned} A(x, t; \xi) &= 1 + A_1(x, \xi)t + A_2(x, \xi)t^2 + O(t^3), \\ \tau(x, t; \xi) &= x \cdot \xi + \tau_1(x, \xi)t + \tau_2(x, \xi)t^2 + O(t^3). \end{aligned} \tag{18}$$

Using (8), we obtain

$$\begin{aligned} A_t(x, t; \xi) &= A_1(x, \xi) + 2A_2(x, \xi)t + 3A_3(x, \xi)t^2 + \dots, \\ \nabla A(x, t; \xi) &= \nabla A_1(x, \xi)t + \nabla A_2(x, \xi)t^2 + \nabla A_3(x, \xi) + \dots, \\ \nabla \tau(x, t; \xi) &= \xi + \nabla \tau_1(x, \xi)t + \nabla \tau_2(x, \xi)t^2 + \dots, \\ \Delta \tau(x, t; \xi) &= \Delta \tau_1(x, \xi)t + \Delta \tau_2(x, \xi)t^2 + \dots, \\ \tau_t(x, t; \xi) &= \tau_1(x, \xi) + 2\tau_2(x, \xi)t + 3\tau_3(x, \xi)t^2 + \dots, \\ \|\nabla \tau(x, t; \xi)\|^2 &= \|\xi\|^2 + 2\xi \cdot \nabla \tau_1(x, \xi)t + \left(\|\nabla \tau_1(x, \xi)\|^2 + 2\xi \cdot \nabla \tau_2(x, \xi) \right) t^2 + \dots \end{aligned} \tag{19}$$

Now we insert the expansions (19) into (5) and (7), and collect the terms of the same order. For the first few terms we obtain,

$$\begin{aligned} \tau_1(x, \xi) &= -V(x) - \frac{1}{2} \|\xi\|^2, \quad \tau_2(x, \xi) = \frac{1}{2} \xi \cdot \nabla V(x), \\ \tau_3(x, \xi) &= -\frac{1}{6} \left[\|\nabla V(x)\|^2 + \xi \cdot \nabla(\xi \cdot \nabla V(x)) \right], \quad A_1(x, \xi) = 0, \\ A_2(x, \xi) &= \frac{1}{4} \Delta V(x), \quad A_3 = -\frac{1}{6} (\nabla(\Delta V(x)) \cdot \xi). \end{aligned}$$

Recursively, we get the following formulae for the coefficients.

If p are integers such that $p \geq 3$:

For an odd p such that $p = 2q + 1$,

$$\tau_p = -\frac{1}{2p} \|\nabla \tau_q\|^2 - \frac{1}{p} \sum_{\substack{k=1 \\ k \neq q}}^{p-2} (\nabla \tau_k \cdot \nabla \tau_{p-1-k}) - \frac{1}{p} \xi \cdot \nabla \tau_{p-1}, \tag{20}$$

and for an even p :

$$\tau_p = -\frac{1}{p} \sum_{k=1}^{p-2} (\nabla \tau_k \cdot \nabla \tau_{p-1-k}) - \frac{1}{p} \xi \cdot \nabla \tau_{p-1}. \tag{21}$$

If p are integers such that $p \geq 2$:

$$A_p = -\frac{1}{p} \left[\left(\xi \cdot \nabla A_{p-1} + \frac{1}{2} \Delta \tau_{p-1} \right) + \sum_{l=1}^{p-2} \left(\nabla \tau_{p-1-l} \cdot \nabla A_l + \Delta \tau_l A_{p-1-l} \right) \right]. \quad (22)$$

From (20), (21) and (22), we can see that the value of each τ_p and A_p depends recursively on the previous ones and the coefficients depend on ∇V only starting from the second coefficient. In particular, if the potential is constant, this Taylor expansion approximation should be exact with no truncation error.

References

- [1] A. Alberucci, M. Peccianti, G. Assanto, Two-color vector solitons in nonlocal media, *Phys. Rev. Lett.* 97 (2006) 153903.
- [2] G. Assanto, M. Peccianti, Spatial solitons in nematic liquid crystals, *IEEE J. Quantum Electron.* 39 (1) (2003).
- [3] G. Assanto, M. Peccianti, C. Conti, Nematicons, *Opt. Photonics News* (2003).
- [4] H.Z. Barakat, J.A. Clark, On the solution of diffusion equation by numerical methods, *J. Heat Transf.* 88 (1966) 421–427.
- [5] E. Braun, L.O. Faucheux, A. Libchaber, Strong self-focusing in nematic liquid crystals, *Phys. Rev. A* 48 (1) (1993).
- [6] E. Braun, L.P. Faucheux, A. Libchaber, D.W. McLaughlin, D.J. Muraki, M.J. Shelley, Filamentation and undulation of self-focused laser beams in liquid crystals, *Europhys. Lett.* 23 (4) (1993) 239–244.
- [7] C.V. Brown, *Physical Properties of Nematic Liquid Crystals*, Springer-Verlag, Berlin, Heidelberg, 2012.
- [8] R. Carles, *Semi-Classical Analysis for Nonlinear Schrödinger Equations*, World Scientific Publishing Co. Pte. Ltd., 2008.
- [9] V. Cervený, M.M. Popov, I. Pšenic, Computation of wave fields in inhomogeneous media – Gaussian beam approach, *Geophys. J. R. Astron. Soc.* 70 (1982) 109–128.
- [10] C. Conti, M. Peccianti, G. Assanto, Route to nonlocality and observation of accessible solitons, *Phys. Rev. Lett.* 91 (7) (2003).
- [11] E.J. Heller, Cellular dynamics: a new semiclassical approach to time-dependent quantum mechanics, *J. Chem. Phys.* 94 (1991) 2723–2729.
- [12] E.J. Heller, Guided Gaussian wave packets, *Acc. Chem. Res.* 39 (2006) 127–134.
- [13] N.R. Hill, Gaussian beam migration, *Geophysics* 55 (1990) 1416–1428.
- [14] M.A. Karpierz, K.A. Brzdakiewicz, Q.V. Nguyen, Modeling of spatial solitons in twisted nematic waveguides, *Acta Phys. Polonica A* 103 (2013).
- [15] I.-C. Khoo, *Liquid Crystals: Physical Properties and Nonlinear Optical Phenomena*, John Wiley & Sons, Inc., 2007.
- [16] E. Kluk, M.F. Herman, H.L. Davis, Comparison of the propagation of semiclassical frozen Gaussian wave functions with quantum propagation for a highly excited anharmonic oscillator, *J. Chem. Phys.* 84 (1986) 326–334.
- [17] B.K. Larkin, Some stable explicit difference approximations to the diffusion equation, *Math. Comput.* 18 (1964) 196–202.
- [18] S. Leung, S. Osher, Alternating Direction Explicit (ADE) Scheme for Time-Dependent Evolution Equations, *UCLA CAM Report* (11-52), 2004.
- [19] S. Leung, J. Qian, An adjoint state method for 3d transmission traveltime tomography using first arrival, *Commun. Math. Sci.* 4 (2006) 249–266.
- [20] S. Leung, J. Qian, Transmission traveltime tomography based on paraxial Liouville equations and level set formulations, *Inverse Probl.* 23 (2007) 799–821.
- [21] S. Leung, J. Qian, Eulerian Gaussian beams for Schrödinger equations in the semi-classical regime, *J. Comput. Phys.* 228 (2009) 2951–2977.
- [22] S. Leung, J. Qian, The backward phase flow and FBI-transform-based Eulerian Gaussian beams for the Schrödinger equation, *J. Comput. Phys.* 229 (2010) 8888–8917.
- [23] S. Leung, J. Qian, R. Burridge, Eulerian Gaussian beams for high frequency wave propagation, *Geophysics* 72 (2007) SM61–SM76.
- [24] S. Leung, J. Qian, S. Susana, Fast Huygen sweeping methods for Schrödinger equations in the semi-classical regime, *Methods Appl. Anal.* 21 (1) (2014) 31–66.
- [25] S. Leung, H.K. Zhao, Gaussian beam summation for diffraction in inhomogeneous media based on the grid based particle method, *Commun. Comput. Phys.* 8 (2010) 758–796.
- [26] D.W. McLaughlin, D.J. Muraki, M.J. Shelley, Self-focussed optical structures in a nematic liquid crystal, *Physica D* 97 (1996) 171–197.
- [27] D.W. McLaughlin, D.J. Muraki, M.J. Shelley, X.P. Wang, A paraxial model for optical self-focussing in a nematic liquid crystal, *Physica D* 88 (1) (1995) 55–81.
- [28] A. Newell, J. Moloney, *Nonlinear Optics*, Addison–Wesley, 1990.
- [29] M. Peccianti, A. De Rossi, G. Assanto, A. De Luca, C. Umeton, I.-C. Khoo, Electrically assisted self-confinement and waveguiding in planar nematic liquid crystal cells, *Appl. Phys. Lett.* 77 (1) (2000).
- [30] J. Qian, S. Leung, A level set based Eulerian method for paraxial multivalued traveltimes, *J. Comput. Phys.* 197 (2004) 711–736.
- [31] J. Qian, S. Leung, A local level set method for paraxial multivalued geometric optics, *SIAM J. Sci. Comput.* 28 (2006) 206–223.
- [32] J. Ralston, Gaussian beams and the propagation of singularities, *Stud. Partial Differ. Equ.* 23 (1983) 206–248.
- [33] J. Rammer, *Quantum Transport Theory*, Perseus Books, Inc., 1998.
- [34] L.S. Schulman, *Techniques and Applications of Path Integration*, Wiley, New York, 1981.
- [35] B.D. Skuse, *The Interaction and Steering of Nematicons*, PhD Thesis, 2010.
- [36] B.D. Skuse, N.F. Smyth, Two-color vector-soliton interactions in nematic liquid crystals in the local response regime, *Phys. Rev. A* 77 (2008) 013817.
- [37] B.D. Skuse, N.F. Smyth, Interaction of two-color solitary waves in a liquid crystal in the nonlocal regime, *Phys. Rev. A* 79 (2009) 063806.
- [38] N. Tanushev, J. Qian, J. Ralston, Mountain waves and Gaussian beams, *SIAM J. Multiscale Model. Simul.* 6 (2007) 688–709.
- [39] X.P. Wang, On the existence of nontrivial solutions for a scalar light-nematic system and its Frederiks transition threshold, *SIAM J. Appl. Math.* 58 (6) (1998) 1852–1861.